Journal of Molecular Structure 1280 (2023) 135025

Contents lists available at ScienceDirect

Journal of Molecular Structure

journal homepage: www.elsevier.com/locate/molstr

A rhodanine derivative as a potential antibacterial and anticancer agent: Crystal structure, spectral characterization, DFT calculations, *Hirshfeld* surface analysis, *in silico* molecular docking and ADMET studies

Amal Guerraoui [a], Meriem Goudjil [b,c], Amani Direm [d,e,*], Abdenour Guerraoui [d,e,*], İlkin Yücel Şengün [f,g], Cemal Parlak [g,h], Amel Djedouani [i,j], Laura Chelazzi [k,l], Filippo Monti [m], Eugenio Lunedei [c], Abdecharif Boumaza [d,e]

[a] *Laboratory of Physics of Radiation and their Interactions with Matter, Faculty of Material Sciences, University of Batna 1, 05000, Algeria*
[b] *Department of Earth Sciences, University of Florence, Via Giorgio La Pira 4, Florence, FI 50121, Italy*
[c] *Consiglio Nazionale delle Ricerche (CNR), Istituto per lo Studio dei Materiali Nanostrutturati (ISMN), Via P. Gobetti 101, Bologna, Italy*
[d] *Department of Matter Sciences, Faculty of Sciences and Technology, Abbes Laghrour University, Khenchela 40.000, Algeria*
[e] *Laboratory of Structures, Properties and Interatomic Interactions LASPI2A, Faculty of Sciences and Technology, Abbes Laghrour University, Khenchela 40.000, Algeria*
[f] *Food Engineering Department, Engineering Faculty, Ege University, Izmir 35040, Turkey*
[g] *Azerbaijan State Agricultural University, AZ-2000, Ganja, Azerbaijan*
[h] *Department of Physics, Faculty of Science, Ege University, Izmir 35040, Turkey*
[i] *Laboratory of Analytical Physicochemistry and Crystallochemistry of Organometallic and Biomolecular Materials, UFMC1, 25000, Constantine, Algeria*
[j] *Higher Normal School of Constantine, University Constantine 3, 25000, Algeria*
[k] *Department of Chemistry "U. Schiff", University of Florence Via della Lastruccia 3-13, Sesto Fiorentino, FI 50019, Italy*
[l] *Centre of Crystallography, University of Florence, Via della Lastruccia 3, Sesto Fiorentino, FI 50019, Italy*
[m] *Consiglio Nazionale delle Ricerche (CNR), Istituto per la Sintesi Organica e la Fotoreattività (ISOF), Via P. Gobetti 101, Bologna 40129, Italy*

ARTICLE INFO

Article history:
Received 12 October 2022
Revised 20 January 2023
Accepted 22 January 2023
Available online 23 January 2023

Keywords:
Rhodanine single crystal
Fluorescence microscopy
DFT
Hirshfeld surface analysis
In silico anticancer and antibacterial inhibitory activity
ADMET properties

ABSTRACT

A novel rhodanine derivative, namely 5-(4-dimethylaminobenzylidene) rhodanine "$C_{12}H_{12}N_2OS_2$", was successfully crystallized from condensation route and characterized by NMR, FT-IR, UV–Vis spectral methods as well as single-crystal X-ray diffraction. This rhodanine derivate crystallizes in the monoclinic $P2_1/c$ space group, with the cell parameters: a = 3.93590(10), b = 11.2480(3), c = 26.6703(7) Å and β = 93.8530(10)°. The molecular structure displays intra- (C – S···H) and intermolecular (N – H···O) hydrogen-bonding interactions. Micro-spectroscopy performed on single-crystals of the studied compound revealed the first absorption transition at 2.25 eV, and a well-structured luminescence peaked at 2.01 eV (0.15 eV broad). Density functional theory (DFT) calculations allowed the structure optimization, the electronic properties, the IR-vibrational modes and frequencies as well as the ^{1}H and ^{13}C NMR chemical shifts' calculation. Furthermore, time-dependent DFT (TD-DFT) calculations were performed for the vertical transition energies. *Hirshfeld* surface analysis (**HSA**) showed the presence of non-conventional C–H···H–C, C–H···π and π···lp interactions and π –π stacking. The anti-cancer and anti-bacterial activities of the studied compound towards the Polo-like kinase PLK1 and the *Escherichia coli* MurB enzymes were *in silico* evaluated by performing molecular docking simulations. The results suggest that the molecule can significantly inhibit the enzymes' active sites. Additionally, the physicochemical and pharmacokinetic characteristics of the molecule were evaluated through absorption, distribution, metabolism, excretion and toxicity (ADMET) analysis, and the results ensure its good drug-likeness properties.

* Corresponding authors.
E-mail addresses: amal.gueraoui@univ-batna.dz (A. Guerraoui), meriem.goudjil@unifi.it (M. Goudjil), direm.amani@univ-khenchela.dz, amani_direm@yahoo.fr (A. Direm), abdenourguerraoui@univ-khenchela.dz (A. Guerraoui), ilkinyucel@yahoo.com (İ.Y. Şengün), cparlak20@gmail.com (C. Parlak), djedouani_amel@yahoo.fr (A. Djedouani), laura.chelazzi@unifi.it (L. Chelazzi), filippo.monti@isof.cnr.it (F. Monti), eugenio.lunedei@cnr.it (E. Lunedei), boumaza.abdecharif@univ-khenchela.dz (A. Boumaza).

https://doi.org/10.1016/j.molstruc.2023.135025
0022-2860/

1. Introduction

Due to their increasing molecular diversity, heterocyclic compounds particularly thiazolidine derivatives have become largely investigated molecules of huge interest in pharmacological and biological industries [1–4]. This exciting class of materials exhibits considerable therapeutic significance, and is used as antiviral, anticonvulsant [1], antimicrobial [5–7], hypolipidaemic and anti-inflammatory agents as well as potential anticancer [8–10], anti-HIV [11, 12], anticonvulsant [13], antidiabetic [14, 15] and calcium-channel blocking [16] drug candidates. For instance, 2-thio-4-ketothiazolidine or 2-thioxo-1,3-thiazolidin-4-one, known also as rhodanine, is one of the intensively studied thiazolidine derivatives [17, 18]. Its derivatives, such as 2-R-, 2-ylidene-4-thiazolidinones, 2-amino(imino)−4-thiazolidinones and 2,4-thiazolidinedione are widely used in the drugs discovery processes [19, 20]. Moreover, the synthetic organic chemists are interested in the benzylidene derivatives of rhodanine because of their broad biological activities [21–23] and therefore the synthesis of rhodanine-based compounds is of considerable interest. Additionally, 5-(4-dimethylbenzylidene amino)rhodanine (DMBAR) is electrophilic and potentially reactive due to possible Michael addition to the exocyclic double bond and thus is considered one of the most biologically active rhodanine derivatives [24]. Moreover, DMBAR is an indicator used for the detection of some metal ions like silver ions [25, 26].

On the other hand, polo-like kinase (PLK) plays an important role in a variety of cellular eukaryotic functions; it is a kind of serine–threonine kinase protein acting as an important regulatory factor in multiple phases of the cellular cycle [27]. There are actually five known protein members of PLK family, namely PLK1, PLK2, PLK3, PLK4 and PLK5 [28–30]. In particular, PLK1 regulates several key steps in the cell's pathway through the G2/M transition and ensures important functions in mitosis including mitotic entry, centrosome assembly, chromosome segregation, spindle assembly checkpoint and cytokinesis [30–39]. The structure of PLK1 is similar to that of other kinase family members, it consists of 603 amino acids [40] and includes an N-terminal Ser/Thr kinase domain and a C-terminal repeat of the polo-box domain (PBD). The phosphorylation of PLK1 is directly related to its enzymatic activity [34]. Interestingly, its over-expression is associated with tumor development, including breast cancer, rectal cancer, colorectal cancer, pancreatic cancer, ovarian cancer and lung cancer, which allows it therefore to serve as a prognostic marker for many cancers [41, 42]. Moreover, it has been the most extensively studied to determine the regulatory mechanisms affecting it and its usefulness as a target for drug design [43].

Recently, theoretical modeling, bioinformatics of functional material and drug design have become much more mature thanks to the advances in computational chemistry. Computational techniques can predict many essential chemical and physical properties of biological and chemical systems [44, 45]. By considering the above studies, we report herein the crystal structure and spectroscopic characterization by means of NMR, FT-IR and UV–Vis of 5-(4-dimethylaminobenzylidene)rhodanine. Additionally, the *Hirshfeld* surface analysis of the molecule has been investigated. In order to gain more insights into the molecular and electronic properties of the studied molecule, the calculations of geometric optimization, frontier molecular orbitals, IR vibration modes and frequencies, ^{1}H and ^{13}C NMR chemical shifts of the compound were performed by DFT, while the excited-state energies were calculated by TD-DFT. Furthermore, we have explored its *in silico* potential to prevent cancer progression by inhibiting the PLK1 enzyme as well as its antibacterial activity against *Escherichia coli* by docking it into the *E. coli* MurB enzyme. Besides, the molecule's drug-likeness was evaluated by *in silico* exploring its ADMET properties.

2. Materials and methods

2.1. Crystallization of the rhodanine derivate

The 5-(4-(dimethylamino)benzylidene)−2-mercaptothiazol-4(5H)-one compound, referred to as (**I**) in all the manuscript, was obtained upon condensation method according to Scheme 1. A few drops of HCl were added to a solution containing bismuth(III) chloride $BiCl_3$ (0.315 g, 0.001 mol) dissolved in 10 mL methanol (MeOH). The solution was stirred for 2 h, after which 15 mL of 5-(4-dimethylamino benzylidene)rhodanine dissolved in MeOH (0.793 g, 0.003 mol) was added dropwise. The obtained solution was refluxed for 4 h, then filtered and left to rest at room temperature. Orange/red elongated rectangular crystals were grown, after a couple of weeks, by slow evaporation of the solution at room temperature. The crystals were recovered from the solution by filtration, and then washed with a small amount of cold ethanol. Yield : 64.25% (0.712 g).

2.2. Single-crystal X-ray diffraction

A suitable crystal, orange/red slab, with dimensions 0.160 × 0.160 × 0.040 mm was selected for single-crystal X-ray diffraction (SC-XRD) experiment. SC-XRD intensity data were collected at T = 150(2) K in a D8 Venture (Bruker-AXS) diffractometer equipped with an IμS 3.0 Incoatec micro-focus source, generating a monochromatic Mo K_α radiation (λ = 0.71073 Å), and a Photon II CPAD detector. Diffraction intensity-data integration and absorption corrections were carried out using SAINT and SADABS software [46]. The *hkl* indexing procedure (with more than 94% of the collected data) revealed a monoclinic cell with cell parameters a = 3.9397 ± 0.0009, b = 11.254 ± 0.003, c = 26.695 ± 0.006 Å and β = 93.843 ± 0.008° The independent reflections (4495 over 41,168 collected) pointed to 2/m Laue group (R_{int} = 0.0575 and R_σ = 0.0372) and the lattice exceptions indicated the *P*-lattice. The intensity statistic tests (Mean |E*E $^{-1}$| = 0.952) suggested a centro-symmetric space group and the systematic absences tests indicated the reflections conditions *h*0*l*: $l = 2n$, 0*k*0: $k = 2n$ and 00*l*: $l = 2n$ in agreement with the $P2_1/c$ space group (R_σ = 0.027) in which the structure solution was undertaken. The crystal structure was solved by intrinsic-phasing method using *SHELXT* program [47] and refined with full-matrix least-squares methods based on F^2 using *SHELXL* program [48]. All non-hydrogen atoms were refined with anisotropic atomic displacement parameters. Hydrogen atoms were located in the Fourier difference map. The final refinement based on F^2 with 4495 unique intensities and 202 parameters converged at $R(F^2)$ = 0.0365 (wR_2 = 0.0907) for 3525 observed reflections with $I > 2\sigma(I)$. The crystal data and structure refinement details are given in Table 1. Olex 2 [49] was used for structure solution and to draw the molecule. CCDC-2196121 contains the supplementary crystallographic data for this paper. These data can be obtained free of charge from the Cambridge Crystallographic Data Centre via https://www.ccdc.cam.ac.uk/data_request/cif.

2.3. NMR measurements

^{1}H and ^{13}C NMR spectra of (**I**) were recorded in DMSO using an Agilent 500 MHz PremiumCompact+ spectrometer (Agilent Technologies Inc., USA). All chemical shifts (δ) are reported in ppm relative to solvent residual peaks. For ^{1}H NMR , J-coupling constants are given in Hz. ^{13}C NMR spectra were acquired with ^{1}H broadband-decoupled mode. To unambigoulsy attribute the resonance signals to specific nuclei, 2D-NMR experiments were also carried out: (i) ^{1}H–^{1}H homonuclear gradient-selected correlation spectroscopy (gCOSY) was used to identify coupled protons;

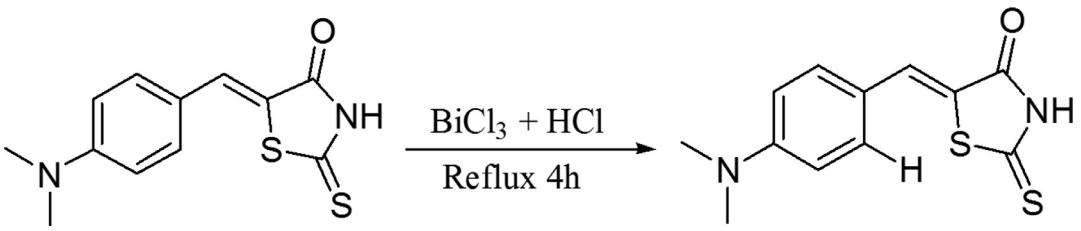

Scheme 1. Crystallization procedure of (**I**).

Table 1
Crystal data, experimental details and structure refinement parameters for (I).

Crystal data	
Chemical formula	$C_{12}H_{12}N_2OS_2$
M_r	264.36
Temperature (K)	150(2)
Crystal system, Space group	Monoclinic, $P2_1/c$
a(Å)	3.93590(10)
b(Å)	11.2480(3)
c(Å)	26.6703(7)
β (°)	93.8530(10)
Volume (Å^3)	1178.05(5)
Z	4
ρ_{calc} (g/cm^3)	1.491
μ (mm^{-1})	0.435
Radiation	Mo $K\alpha$ ($\lambda = 0.71073$)
Crystal size (mm^3)	0.160 × 0.160 × 0.040
Data collection	
2θ range (°)	3.93–66.47
F(000)	552
$(\sin\theta/\lambda)_{max}$ (Å^{-1})	0.771
Index ranges	$-6 \le h \le 6$ $-17 \le k \le 17$ $-40 \le l \le 41$
$T_{min}-T_{max}$	0.709–0.747
Reflections collected	41,168
Independent reflections	4495
Observed reflections with [$I > 2\sigma(I)$]	3525
R_{int}	0.0575
R_{sigma}	0.0372
Refinement	
Data/restraints/parameters	4495/0/202
Final R indexes [$F^2 > 2\sigma(F^2)$]	$R = 0.0365$, $R_w = 0.0857$
Final R indexes [all data]	$R = 0.0538$, $R_w = 0.0907$
Goodness-of-fit on F^2	1.043
Largest diff. peak/hole (e.Å^{-3})	+0.40/−0.31

(ii) Nuclear overhauser enhancement spectroscopy (NOESY) was adopted to trace out hydrogens nuclei close in space; (iii) ^{1}H–^{13}C heteronuclear single-quantum 1-bond J-correlation spectroscopy with adiabatic 180° pulses and gradient-coherence selection (gHSQCAD) was used to correlate protons with directly attached carbons; (iv) ^{1}H–^{13}C heteronuclear multiple-bond J-correlation spectroscopy with adiabatic 180° pulses and gradient-coherence selection (gHMBCAD) was exploited to correlate protons with carbons at (2- or) 3-bond distances, which turned out to be extremely useful to unambigously identify all the five quaternary carbons of (**I**). For all 2D experiments, non-uniform sampling (NUS) at 50% was chosen as acquisition method to maximize the spectral resolution *vs.* acquisition time ratio; the Modified Iterative Soft Threshold algorithm (MIST) was used for the reconstuction of NUS data, as implemented in MestreNova. ^{1}H NMR (500 MHz, DMSO) δ: 13.55 (s, 1H), 7.51 (s, 1H), 7.43 (d, J = 9.1 Hz, 2H), 6.83 (d, J = 9.1 Hz, 2H), 3.03 (s, 6H). ^{13}C NMR (126 MHz, DMSO) δ: 195.26, 169.91, 151.76, 133.04, 132.88, 119.88, 117.77, 112.22, 39.62.

2.4. Infrared measurements

A 2 mg amount of crystals of (**I**) was ground and diluted in 100 mg of dried spectroscopic grade KBr and pressed in a vacuum die under a pressure of 10 tons. Mid-IR vibrational spectrum was recorded in transmission mode in the range 370–7500 cm^{-1} at a resolution of 4.0 cm^{-1} using a Bruker Vertex 70 FT-IR spectrometer, with a CO_2 and H_2O purging system.

2.5. Optical measurements

2.5.1. UV–visible absorption in solution

The absorption spectrum of (**I**) was recorded in ethanol (EtOH) in the wavelength range 200–900 nm (with bandwidth: 2.0 nm and scan speed: 100 nm/min) using a Jasco-550 UV–Vis spectrophotometer. The solution was prepared in the 10^{-5} M concentration.

2.5.2. Single-crystal optical absorption and emission micro-spectroscopy

Absorption and emission spectra of single crystals of (**I**), as well as their fluorescence images, were recorded by means of a modified Nikon Eclipse80i epifluorescence microscope. Its standard trinocular turret was customized, in its superior part, in order to mount a homemade optical system (composed of a 50 mm focal quartz lens focused into a UV–Vis optical fiber bundle, Thorlabs) to feed the optical signal from microscope into an Avantes AvaSpec-2048 CCD spectrometer (2048 pixels array, DLC UV–Vis, 200–1100 nm range, 10 μm entrance slit, software programmed). This allowed us recording fluorescence images and collecting the transmitted (for absorption) or emitted (for photoluminescence) signal from single crystals of (**I**), under a 20X–100X objective. In transmission mode, the built-in Nikon bottom halogen lamp was used (white light, illumination range 400–1000 nm). The lamp light passed across the crystal was then collected through the microscope objective, and fed into the spectrometer fiber. For the photoluminescence spectra, a top mounted OSRAM Mercury Short Arc lamp (HBO) 100 W, was properly energy filtered to provide a suitable excitation (λ_{exc} = 380–436 nm) and its light brought to excite the crystals across the microscope objective. The fluorescence signal, collected back across the same objective, was eventually fed into the spectrometer via optical fiber after having passed

through a dichroic mirror and an exit filter to suppress residual excitation straylight. In this way, it was possible, within the same experimental session, selecting the more suitable crystals by visual inspection under strong magnification, and then recording a bright-field microimage, followed by a fluorescence image and successively measuring the local micro-absorption in transmission mode and the local micro-fluorescence spectrum. Fluorescence images were collected by means of a Nikon DigitalSight DS-2 M camera, using a 436 nm excitation filter, a 455 nm dichroic mirror and a 475 nm long-pass exit filter. Integration time was of the order of few seconds (1 – 10 s) for the fluorescence spectra and between 1/100 and 1/8 of second for fluorescence images.

2.6. Computational details

The geometry of (**I**) was fully optimized using DFT in the gas phase by using the ***B3LYP*** functional in conjunction with the ***cc-pvdz*** and **6–311+*G*(*d*,*p*)** basis sets. In addition, the vibrational wavenumbers and the frontier molecular orbitals were calculated and the vibrational frequencies were scaled by 0.9970 for the ***B3LYP*/6–311+*G*(*d*,*p*)** level [50]. TD-DFT calculations were carried out using ***CAM-B3LYP*** and ***BLYP*** levels of theory. Two basis sets, namely **6–311+*G*(*d*, *p*)** and ***TZVP***, were chosen for each method. TD-DFT calculations were completed in ethanol by the polarizable continuum method [51] and performed by the Tamm-Dancoff approximation (TDA) [52]. After structure optimization at ***B3LYP*/6–311+*G*(*d*,*p*)** level in DMSO, ^{1}H and ^{13}C NMR chemical shifts (δ_H and δ_C) were calculated using the GIAO method [53] in DMSO at the same level. NMR chemical shifts were scaled with default values of TMS in GaussView [54], which was used to visualize the examined structure. All calculations were performed using Gaussian 09 software [55].

2.7. Hirshfeld *surface analysis*

The *Hirshfeld* surfaces (**HS**s) and their related 2D-fingerprint plots (**FP**s) were obtained using CrystalExplorer21 software [56]. The **HS** was mapped over d_{norm}, d_i and *shape index* functions, respectively in the range of [−0.5807 to 0.9819 Å], [0.7555 to 2.4505 Å] and [−1.000 to 1.000 Å].

2.8. Molecular docking

Molecular docking analysis is a computational technique aiming to explore possible binding modes of ligands to receptors. The *in silico* studies were carried out using AutoDock4.2 software and AutoDock Tools ADT [57]. The X-ray crystal structures of the targets were obtained from the Research Collaboratory for Structural Bioinformatics (RCSB) protein data bank [58] with the following Protein Data Bank (PDB) IDs: **2Q85** and **4J7B**, for respectively Polo-like kinase 1 (PLK1) and *E. coli* MurB enzyme. Moreover, the interacting residues involved in the binding pockets of the resulting docked complexes were evaluated and analyzed using Discovery Studio Visualizer 2021 [59].

2.9. ADMET analysis

An *in silico* ADME profile, in terms of absorption, distribution, metabolism and excretion, was computed for compound (**I**) prior to that it could be destined for preclinical trials and *in vivo* studies. The results were obtained with the SwissADME web tool [60], which provides free access to predictive physicochemical properties, pharmacokinetics, drug-likeness and medicinal chemistry friendliness. As for the toxicity of (**I**), it was generated using the web server admetSAR 1.0 (http://lmmd.ecust.edu.cn/admetsar1) [61], which predicts the values of the human Ether-a-go-go-related gene inhibition, the Ames toxicity, the acute oral toxicity and the carcinogenicity of the studied molecule.

3. Results and discussion

3.1. X-ray crystallographic study

Compound (**I**) crystallizes in the monoclinic $P2_1/c$ space group. Its asymmetric unit is composed of one rhodanine derivative molecule. The Ortep diagram with thermal ellipsoids drawn at 50% probability illustrating the asymmetric unit of (**I**) is shown in Fig. 1.

The C—H bond of the phenyl ring is linked to the thiazolidine ring's sulfur *via* a short intramolecular C6—H6···S2 hydrogen bond, with a distance of 2.517 Å, resulting in a $S(6)$ ring motif [62] which plays a decisive role in the stabilization of lattice compounds [63, 64]. This value compares well with the C—H···S bond lengths observed in similar compounds [65, 66]. For instance, this bond distance agrees with the one reported in (Z)−3-allyl-5-(3-bromobenzylidene)−2-sulfanylidene-1,3-thiazolidin-4-one [65] which is 2.52 Å. However, this distance is slightly longer than the ones observed in [67] and [68], which are equal respectively to 2.50 Å and 2.48 Å. Moreover, it is shorter than the one found in the published work by Balakumaran et al. [63] with a value of 2.63 Å.

The dihedral angle between the rhodanine and the phenyl rings is slightly inclined (7.13(12)°). Also, the exocyclic angles S2—C3—C4 and C4—C5—C6 (128.83° and 125.06°) are significantly larger than the angles C2—C3—C4 and C4—C5—C10 (121.89° and 118.54°), which indicates that the intramolecular C6—H6···S2 interaction is strongly repulsive [69]. Furthermore, the crystal packing of (**I**) displays intermolecular H-bonds, namely the strong N—H···O of 2.848 Å connecting the thiazolidine's azote N1 as a donor to the ketone's O1 as an acceptor, leading to the ring $R_2^2(8)$ graph-motif as displayed in Fig. 2.a.

In addition, we noticed the presence of two non-covalent $\pi-\pi$ stacking, namely the π(S) $-\pi$(C = O) and phenyl···phenyl interactions with the respective distances of 3.486 and 3.394 Å (Fig. 2.b). The hydrogen-bonding networks in (**I**) are highlighted in Fig. 2.c and Table 2.

3.2. Molecular geometry

The structure of (**I**) was optimized using DFT at the ***B3LYP*/*cc-pvdz*** and ***B3LYP*/6–311++*G*(*d*,*p*)** levels of theory. Selected calculated values of the geometric parameters were compared to the experimental ones and are listed in Table 3. The experimental bond lengths are between 1.2255(15) and 1.7525(12) Å, with the mean value being ⟨1.4467 Å⟩. Similarly, the optimized values of bond lengths are in the range [1.218−1.777] Å for ***B3LYP*/*cc-pvdz*** and [1.213−1.776] Å for the ***B3LYP*/6–311++*G*(*d*,*p*)** level of theory, with the respective average bond lengths of ⟨1.457 Å⟩ and ⟨1.453 Å⟩. As for the experimental bond angles, they vary from 92.98(6) to 130.58(11)° with an average value of ⟨115.84°⟩. Correspondingly, the theoretical bond angles' values were found to vary from 92.74 to 132.34° for ***B3LYP*/*cc-pvdz*** and 92.74 to 132.22° in the case of ***B3LYP*/6–311++*G*(*d*,*p*)**, which corresponds to the related mean values ⟨119.65°⟩ and ⟨119.75°⟩, respectively. Fig. 3 illustrates the graphical distribution correlations giving R^2 factors of 0.99 for the bond distances and angles of (**I**), which indicates that the calculated values are in a good agreement with the experimental results. Furthermore, both basis sets reproduce well the geometric parameters, however the results of **6–311+*G*(*d*,*p*)** are slightly in a better agreement with the experimental values and it will be thus adopted for the following calculations.

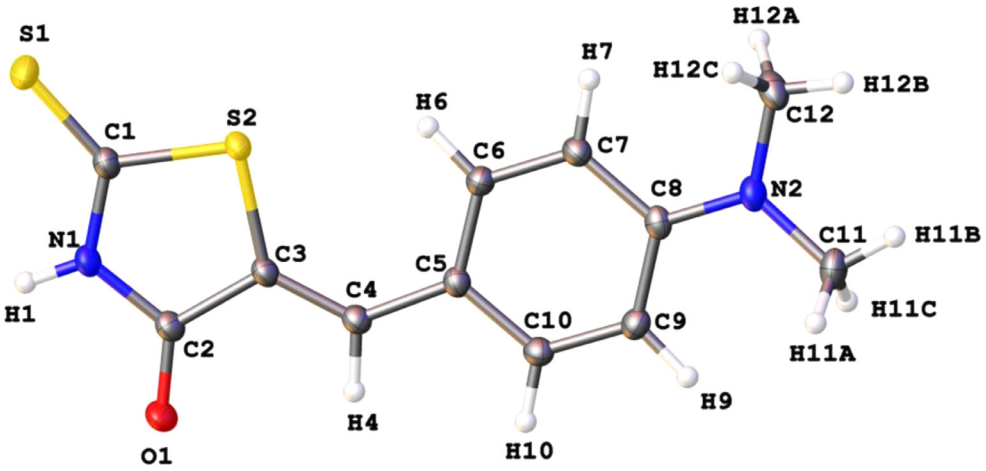

Fig. 1. Asymmetric unit of (**I**) drawn with thermal ellipsoids at 50% probability.

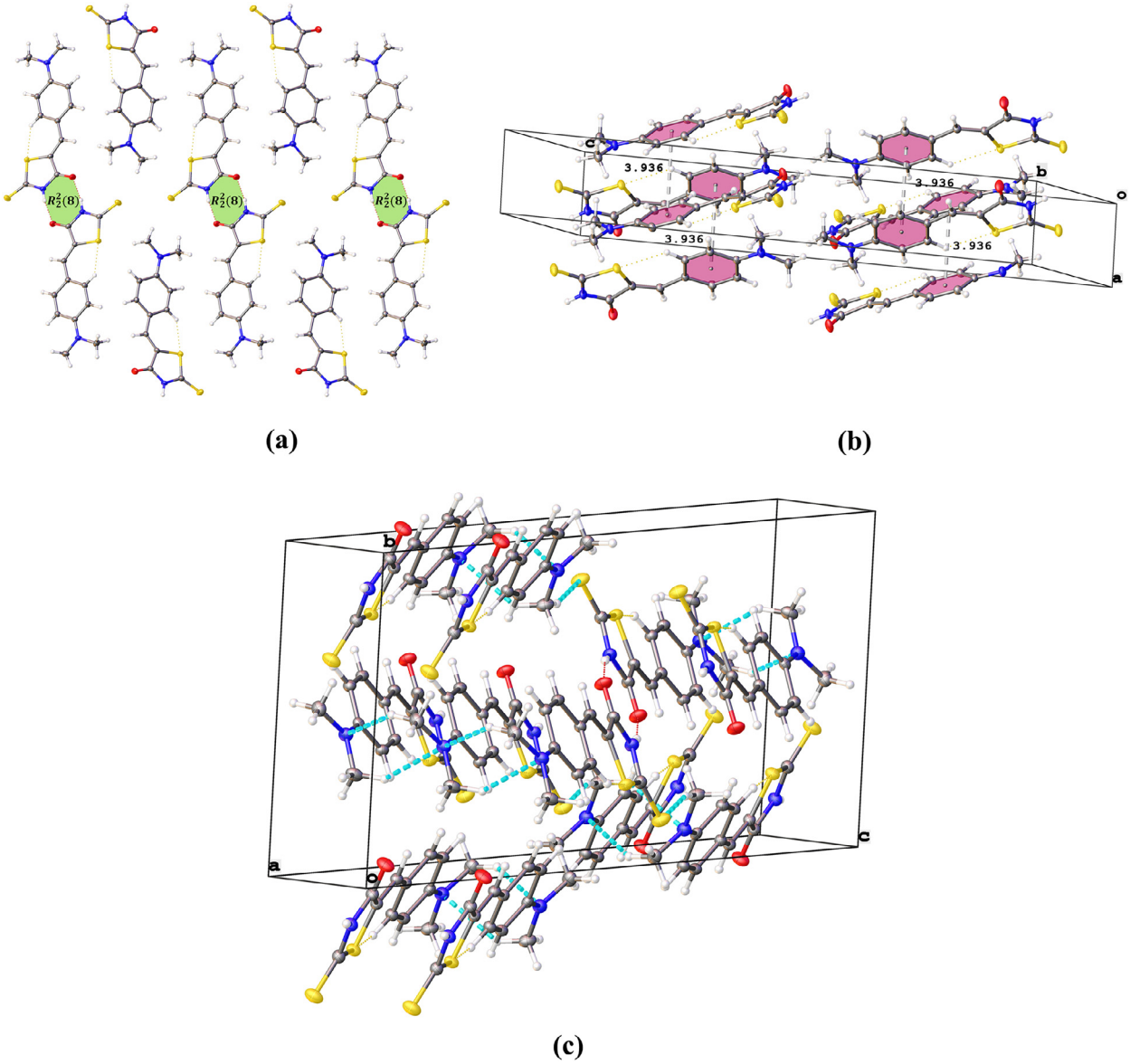

Fig. 2. **(a)** $R^2_2(8)$ ring graph motifs resulting from the N—H···O hydrogen bonds, **(b)** $\pi-\pi$ stacking and **(c)** H-bonding networks in (**I**).

Table 2
Hydrogen bonds' geometry (Å, °) in compound (**I**).

D—H···A	D—H	H···A	D···A	D—H···A
C6—H6···S2	0.992	2.517	3.230	128.59
N1—H1···O1	0.881	1.983	2.847	166.58
N1—H1···O1^{i}	0.881	1.983	2.847	166.58
C4—H4···H12C^{ii}	0.985	2.267	3.232	166.10
C12—H12B···S1^{iii}	0.955	2.927	3.857	164.89
C11—H11C···S2^{iv}	0.983	2.906	3.866	165.73
C12—H12A···C8^{v}	1.019	2.818	3.665	140.78
C12—H12A···N2^{v}	1.019	2.737	3.526	134.88

Symmetry codes : (i) : $-x, 1-y, 1-z$, (ii) : $1-x, -\frac{1}{2}+y, \frac{3}{2}-z$, (iii) : $1+x, \frac{3}{2}-y, \frac{1}{2}+z$, (iv) : $2-x, -\frac{1}{2}+y, \frac{3}{2}-z$, (v) : $1+x, y, z$.

Table 3
Experimental and theoretical geometric parameters, bond lengths (Å) and bond angles (°), in compound (**I**).

No.	Bond	Exp	Theoretical *B3LYP*		No.	Bond	Exp	Theoretical *B3LYP*	
			cc-pvdz	**6–311++*G*(*d*,*p*)**				***cc-pvdz***	**6–311++*G*(*d*,*p*)**
1	S1—C1	1.6289 (13)	1.6473	1.6443	10	C2—C3	1.4722 (16)	1.4794	1.4793
2	S2—C1	1.7525 (12)	1.7775	1.7736	11	C3—C4	1.3544 (17)	1.3584	1.3555
3	S2—C3	1.7514 (13)	1.7768	1.7765	12	C4—C5	1.4385 (17)	1.4425	1.4413
4	O1—C2	1.2255 (15)	1.2179	1.2131	13	C5—C6	1.4062 (17)	1.4129	1.4109
5	N1—C1	1.3646 (16)	1.366	1.3659	14	C5—C10	1.4107 (17)	1.4131	1.4113
6	N1—C2	1.3851 (16)	1.4056	1.403	15	C6—C7	1.3749 (17)	1.3831	1.3813
7	N2—C8	1.3611 (16)	1.3747	1.3724	16	C7—C8	1.4177 (17)	1.4194	1.4179
8	N2—C11	1.4545 (18)	1.4546	1.4558	17	C8—C9	1.4150 (17)	1.4184	1.417
9	N2—C12	1.4520 (18)	1.4549	1.4562	18	C9—C10	1.3752 (18)	1.3825	1.3806
No.	**Angles**	**Exp**	**Theoretical *B3LYP***		**No.**	**Angles**	**Exp**	**Theoretical *B3LYP***	
			cc-pvdz	**6–311++*G*(*d*,*p*)**				***cc-pvdz***	**6–311++*G*(*d*,*p*)**
1	C3—S2—C1	92.98 (6)	92.7433	92.7339	14	C4—C3—C2	121.88 (11)	120.0149	120.4403
2	C1—N1—C2	118.00 (10)	119.8074	119.6869	15	C3—C4—C5	130.58 (11)	132.3433	132.2192
3	C8—N2—C11	120.53 (11)	120.1007	120.2228	16	C6—C5—C4	125.05 (11)	125.3666	125.368
4	C8—N2—C12	120.68 (11)	120.2584	120.3927	17	C6—C5—C10	116.38 (11)	116.4599	116.4335
5	C12—N2—C11	118.29 (11)	119.641	119.3845	18	C10—C5—C4	118.54 (11)	118.1735	118.1984
6	S1—C1—S2	122.82 (7)	124.8363	124.6903	19	C7—C6—C5	122.06 (11)	121.8771	120.5261
7	N1—C1—S1	127.72 (10)	126.574	126.5821	20	C6—C7—C8	121.18 (11)	121.2776	121.3076
8	N1—C1—S2	109.46 (9)	108.5897	108.7276	21	N2—C8—C7	121.02 (11)	121.3578	121.3997
9	O1—C2—N1	123.30 (11)	123.1525	123.1109	22	N2—C8—C9	121.82 (11)	121.4636	121.4962
10	O1—C2—C3	126.46 (12)	127.947	127.9051	23	C9—C8—C7	117.16 (11)	117.1786	117.104
11	N1—C2—C3	110.23 (10)	108.9005	108.9841	24	C10—C9—C8	120.66 (11)	120.7442	120.4242
12	C2—C3—S2	109.30 (9)	109.9591	109.8675	25	C9—C10—C5	122.52 (11)	122.4626	122.4767
13	C4—C3—S2	128.80 (9)	130.026	129.6923					

3.3. NMR characterization

The ^{1}H and ^{13}C NMR spectra of (**I**) are reported in Figure S1 and S4 (see Supplementary Material File), and are both fully consistent with the proposed molecular structure. In order to properly assign each of the NMR peaks to the corresponding nuclei, gCOSY (Figure S2), NOESY (Figure S3), gHSQCAD (Figure S5), and gHMBCAD (Figure S6) have been also carried out. Fig. 4 summarises the experimental findings. On the other hand, the theoretical ^{1}H and ^{13}C NMR chemical shifts of the studied compound were calculated using the ***B3LYP*/6–311+*G*(*d*,*p*)** basis set. Therefore, the chemical shifts of the carbons C1-C9 were found to be 41.18, 157.37, 115.90, 139.61, 124.30, 140.90, 124.60, 207.3 and 172.35 ppm. Whereas, the related values for H_{Me}, H_a, H_b, H_c and H_d were computed as 3.11, 6.81, 7.60, 7.70 and 8.39 ppm, respectively. According to the obtained results, it can be concluded that the calculated chemical shifts agree well with the experimental values, with the mean absolute errors between the experimental and theoretical ^{1}H and ^{13}C NMR chemical shifts found to be 1.12 and 5.57, respectively.

3.4. Vibrational band assignments

The experimental (red line) and ***B3LYP*/6–311++*G*(*d*,*p*)** computed infrared (blue line) spectra of (**I**) are given in Fig. 5. The band appearing at around 3440 cm^{-1} in the experimental spectrum and at 3588 cm^{-1} in the theoretical spectrum indicates the symmetric stretching (ν_s) of the N—H bond. Its wide shape is due to its implication in the formation of intermolecular hydrogen bonds [70]. In the experimental spectrum, we noticed the presence of a band at 3120 cm^{-1} which could be attributed to the C—H stretching of the phenyl ring [71], whereas it appears at 3189 cm^{-1} in the calculated spectrum. As for the bands observed at 2906 and 3027 cm^{-1}, they are respectively attributed to the asymmetric and symmetric stretching ν_{as}(C—H) and ν_s(C—H) of the methyl group. Correspondingly, the computed values are found to be respectively 2992 and 3035 cm^{-1}. The stretching of the carbonyl group C = O is associated with the band at 1685 cm^{-1} in the experimental spectrum [72] and around 1764 cm^{-1} in the computational ones. The experimental sharp peaks at 1568 and 1526 cm^{-1} and the ones ob-

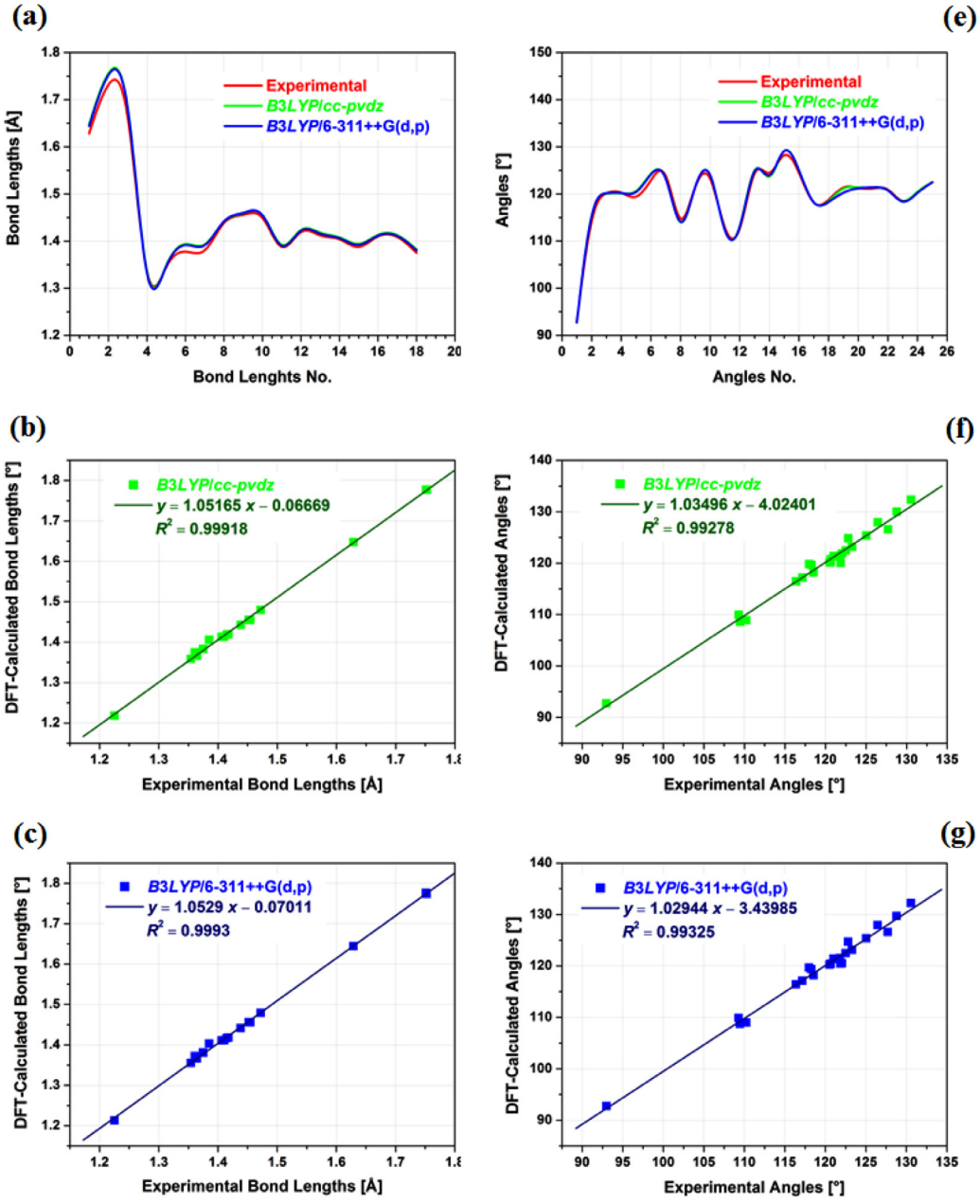

Fig. 3. Correlation curves between experimental and computed geometric parameters for compound (**I**).

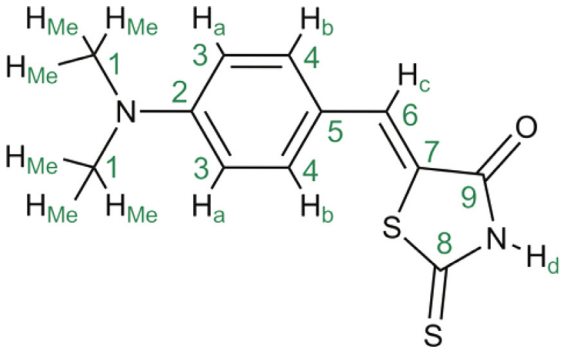

δ(H$_{Me}$) = 3.03 ppm
δ(H$_a$) = 6.83 ppm
δ(H$_b$) = 7.43 ppm
δ(H$_c$) = 7.51 ppm
δ(H$_d$) = 13.55 ppm

δ(C1) = 39.62 ppm
δ(C2) = 151.76 ppm
δ(C3) = 112.22 ppm
δ(C4) = 132.88 ppm
δ(C5) = 119.88 ppm
δ(C6) = 133.04 ppm
δ(C7) = 117.77 ppm
δ(C8) = 195.26 ppm
δ(C9) = 169.91 ppm

Fig. 4. Resolved NMR structure of (**I**) in DMSO–d6. Chemical shifts (δ) are reported relative to DMSO residual peaks.

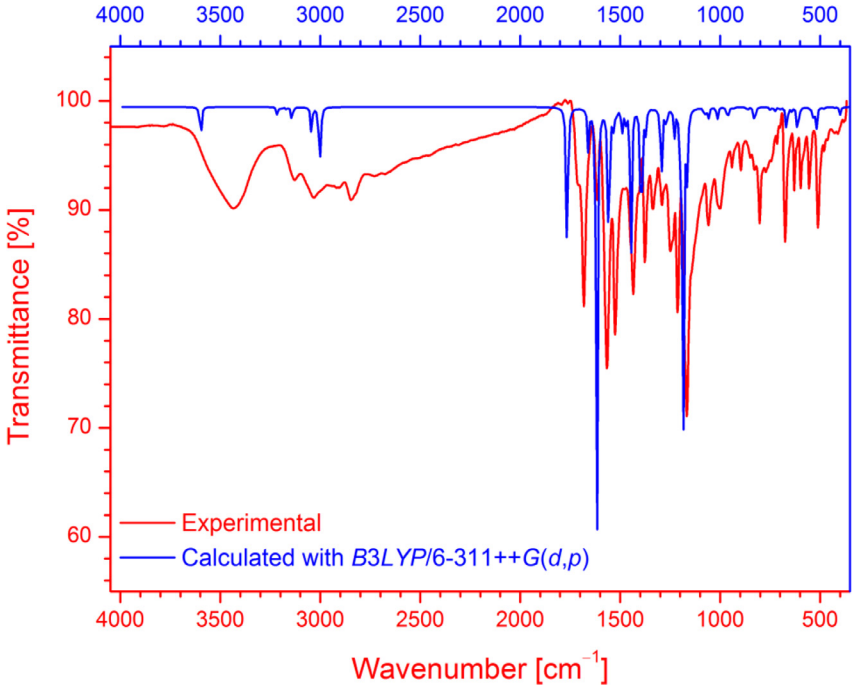

Fig. 5. Experimental and theoretical IR spectra of (**I**).

served at 1654 and 1612 cm^{-1} in the calculated IR spectrum are assigned to the C = C stretching of the phenol ring. While, δ(C—N) and δ(N—H) bending modes are both observed at 1428 cm^{-1} and calculated at 1441 cm^{-1} [73]. Furthermore, the δ(C—H) bending was recorded at 1378 cm^{-1} and computed at around 1370 cm^{-1}. As for the bands observed at 1219 and 1240 cm^{-1}, in the experimental spectrum, they could be attributed to the thio-carbonyl group (C = S) stretching. Similarly, the related computed values were found to be 1224 and 1278 cm^{-1}. On the other hand, the bending of the same group was observed at 634 cm^{-1} [74] and calculated to be at 665 cm^{-1}.

3.5 UV–vis absorption and luminescence characterization

Crystals of (**I**) consist of regular, rigid, elongated thin slabs, orange/red in color with their longer dimension in the order of ∼(0.3 − 1.5 mm) and their transversal one of ∼(50−150 μm). By making use of the setup described in Section 2.5.2, we carried out a local micro-characterization, which allowed us to collect absorption and emission signals from an area of the crystal down to 30 μm in diameter. Absorption was measured (in transmission mode) across the crystal, by collecting the spectrum in various positions to test the homogeneity of the signal. We used a white-light broad-spectrum halogen lamp to illuminate from below the crystal. Fig. 6.a shows a typical crystal of (**I**) (approx. ∼1500 μm × 150 μm in dimension) as appears, at low magnification, during the measurement. By increasing the objective power and making use of a diaphragm, it is possible to select a limited portion of the crystal surface, for collecting and spectrally resolving the light crossing the crystal. The local absorption is computed from the crystal transmittance with respect to the reference transmittance of the background (UV glass).

Fig. 6.b shows the same crystal during a fluorescence experiment. The crystal is epi–illuminated by a monochromatized Hg lamp through the microscope objective; the orange/red glow visible in the image is the luminescence signal, upon excitation at λ_{exc} = 436 nm. The detection area is indicated by the small dashed circle (diameter ∼50 μm). Fig. 6.c shows, on the same energy scale, the absorption and fluorescence spectra as measured in the indicated position. The absorption, polarized along the long crystalline axis, appears to be rather unstructured. It exhibits a sharp onset at around 2.0 eV (620 nm) and three convoluted broad features at 2.25 eV (550 nm, assigned to lowest energy transition in solid state), at 2.58 eV (480 nm) and at 2.92 eV (425 nm). Noticeably, the crystalline form of (**I**) turns out to be strongly relaxed in energy with respect to the molecule in solution, laying the crystal absorption onset 1.62 eV lower in energy than the $\pi-\pi^*$ electronic transition in solution (320 nm, 3.87 eV), and 0.50 eV lower than the donor-acceptor intramolecular charge transfer (450 nm, 2.75 eV), see Figure S7. The vertical transition energies were calculated and compared with experimental data. For this process, different levels of theory were used since TD-DFT/TDA have limitations for calculations of both adiabatic and non-adiabatic transitions [52]. The combination method ***CAM-B3LYP*** with the two basis sets **6–311+*G(d,p)*** and ***TZVP*** has higher oscillator strength but transient energies are over-estimated (3.06 eV (%93) and 3.25 eV (%93) with 1.1625 and 1.4285 osc. strengths). However, ***BLYP/TZVP*** produces two vertical transitions which cover experimental observation with different percentages (2.53 (%83) eV and 3.32 (%12) eV with 0.8610 and 0.7168 osc. strength) with relatively high oscillator strengths. The mean value of the two transition energies is quite close to the experimental data.

As a characteristic of organic molecular crystals, their fluorescence is usually well structured. This reflects the fact that the molecular character is retained in solid state, owing to the weakness of hydrogen bond/Van der Waals interactions among the molecules in the crystal. The crystal fluorescence of (**I**), traced in red in Fig. 6.c, has a peak at 2.01 eV (615 nm), with a FWHM of ∼150 meV. The emission is strongly polarized along the long crystalline axis. The apparent Stokes shift (SSh) amounts to ∼1950 cm^{-1} (∼0.24 eV, $\Delta\lambda$ ∼65 nm). Crystal fluorescence exhibits a structured vibronic progression built on a vibrational mode of energy ∼1240 cm^{-1} (0.155 eV), which could be associated to the strong stretching mode of the thio-carbonyl group (C = S) experimentally detected at a similar energy (see Fig. 5).

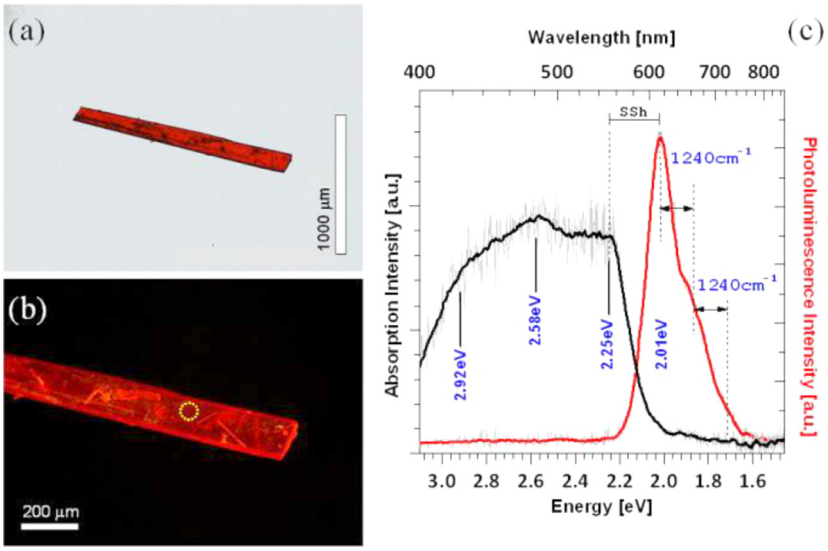

Fig. 6. **(a)** Bright-field microimage of crystal of **(I)**, in white-light bottom illumination. **(b)** Fluorescence micro-image of the same crystal, at a stronger magnification. The intense orange/red signal is the luminescence excited at λ_{exc} = 436 nm. The small dashed circle (diameter ∼50 μm) indicates the selected area from where both the transmittance and the luminescence signals have been collected. **(c)** Local micro-absorption and micro-fluorescence spectra as measured inside the aforementioned selected area. The spectral positions of the main features are reported on the plot. SSh indicates the observed Stokes shift of ∼1950 cm^{-1} (∼0.24 eV, $\Delta\lambda$ ∼65 nm). Luminescence, peaked at 2.01 eV, exhibits a vibronic progression built on a vibrational mode of energy ∼1240 cm^{-1} (0.155 eV). See text for details.

3.6. Frontier molecular orbitals analysis

It is indicated in the frontier molecular orbitals' (FMOs) calculations that the higher the E_{HOMO} is, the greater the electron donating capacity will be and the lower the E_{LUMO} is, the smaller the resistance to accept electrons will be [75]. In addition, the energy gap $\Delta E_{(HOMO-LUMO)}$ is considered significant for the biological activity of molecules [76, 77]. Thus, molecules with a large energy band gap have smaller chemical reactivity than those with a lower energy band gap [78]. The values of HOMO and LUMO energies of the studied compound calculated by ***B3LYP*/6–311++*G*(*d*,*p*)** level of theory are illustrated in Fig. 7.

The HOMO orbitals in (**I**), which relate to the highest density of negative charges, are mainly located on the thio-amide ring fragment and on the exocyclic sulfur atom and originated from double bonds and unshared electron pairs. Whereas, the LUMO ones are situated on the phenyl ring fragment of the studied molecule. The computed values of E_{HOMO} and E_{LUMO} obtained by ***B3LYP*/6–311++*G*(*d*,*p*)** are respectively found to be −5.6890 eV and −2.5504 eV. As for the energy gaps between the HOMO and LUMO orbitals, the same level of theory gave the following value 3.1386 eV. This band gap could indicate a high conductivity of compound (**I**). The calculated chemical reactivity descriptors of (**I**), such as the absolute electronegativity (χ), the absolute hardness (η), the chemical potential (μ), the absolute softness (S), the global electrophilicity (ω) and the additional electronic charge ΔN_{max}, are given in Table 4.

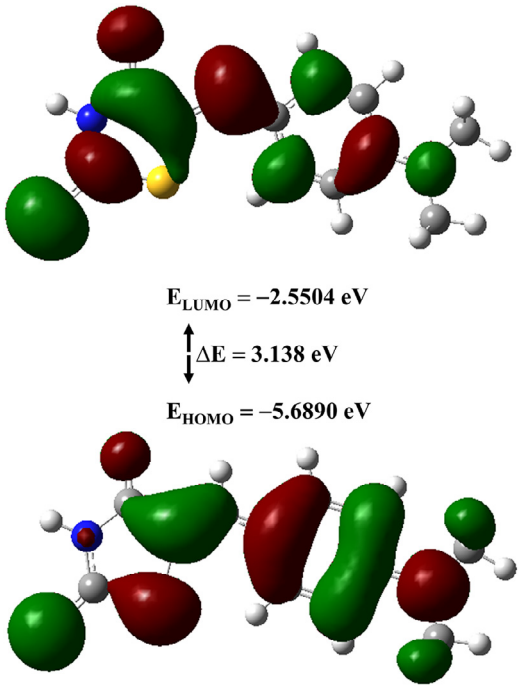

Fig. 7. Frontier molecular orbitals in compound (**I**) obtained by ***B3LYP*/6–31++*G*(*d*,*p*)** theory level.

3.7. Hirshfeld *surface analysis (HSA)*

To gain more information about the interactions in the molecular crystal of (**I**), a **HSA** was performed in which the surface was mapped over d_{norm} as shown in Fig. 8.a. The red spots on the front and back surface of the molecule indicate the interactions with distances shorter than the sum of the *van der Waals* radii. Consequently, two big red regions are observed on the d_{norm} function and are related to the H···O/O···H contacts which could be associated to the reciprocal N1—H1···O1/O1···H1—N1 hydrogen bonding interactions. In addition, faint red spots, appearing on the **HS** of Fig. 8.a, result from the C11—H11C···S2 and C12—H12B···S1 interactions originating from the H···S/S···H contacts. In Fig. 8.b, we have mapped the **HS** of (**I**) over the d_i representation which shows the presence of the reciprocal C4—H4···H12C—C12/C12—H12C···H4—C4 interactions resulting from the H···H contacts.

Additionally, the mapping of the *shape index* function on the *Hirshfeld* area of (**I**) allowed to display the H···π interactions identified as red-blue triangles highlighted in Fig. 9.

Once established, the decomposed fingerprint plots **FPs** gave a quantitative summary of all the intermolecular contacts in the crystal, which enabled the analysis of the individual contribution of each of the existing contacts (Fig. 10). The H···H contacts are

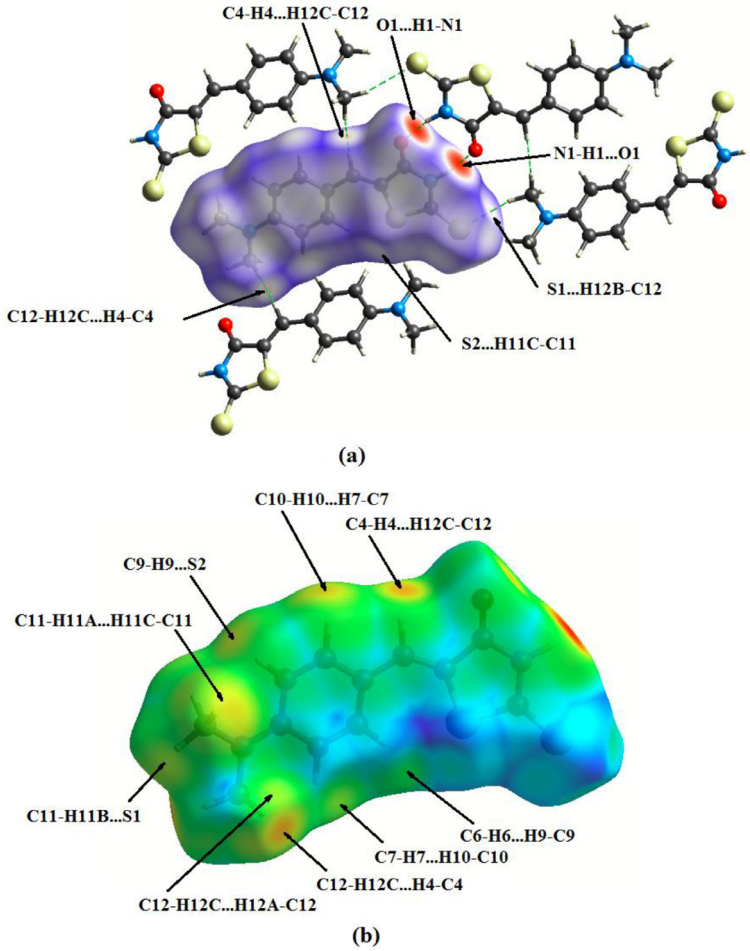

Fig. 8. 3D *Hirshfeld* maps mapped on **(a)** d_{norm} and **(b)** d_i showing the related interactions.

Table 4
Calculated reactivity parameters (eV) of (**I**).

	B3LYP/6–31++*G*(*d*,*p*)
$A = -E_{LUMO}$	2.5503
$I = -E_{HOMO}$	5.6891
ΔE	3.1386
	4.1197
Electronegativity (χ)	
Hardness (η)	1.5694
Softness (S)	0.31859
Chemical potential (μ)	−4.1197
Electrophilicity (ω)	5.4061
Fraction of the transferred electrons (ΔN_{max})	2.62501

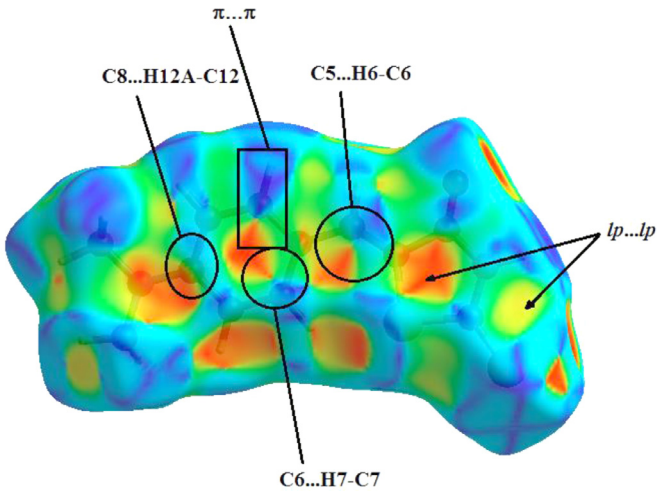

Fig. 9. *Shape index* of (**I**) showing the H···π interactions.

considered the major contributor to the crystal packing of (**I**), with a percentage of 32.9% (Fig. 10.a). This category shows a shortest contact resulting from the C4—H4···H12C—C12 interaction and appearing in the 2D-**FP** at about d_i = 1.12 Å and d_e = 1.14 Å. Furthermore, the S···H/H···S contacts are one of the most frequent in (**I**) and contribute with a value of 23.1%. Correspondingly, the shortest contacts are indeed attributed to the C12—H12C···S1 and C11—H11C···S2 interactions, which respectively appear at $d_i + d_e$ values of around 2.87 and 2.9 Å (Fig. 10.b). Moreover, we have illustrated in (Fig. 10.c) the 2D-**FP** of the H···C/C···H contacts' contribution, being 16.1% of the total **HS**, with a shortest contact situated at approximately $d_i + d_e$ ~2.8 Å which is associated to the C12—H12A···π interaction involving the aromatic C8 atom. As for the H···O/O···H contacts, they account for 10.8% and are displayed as two long symmetric spikes in the middle of the **FP** of Fig. 10.d,

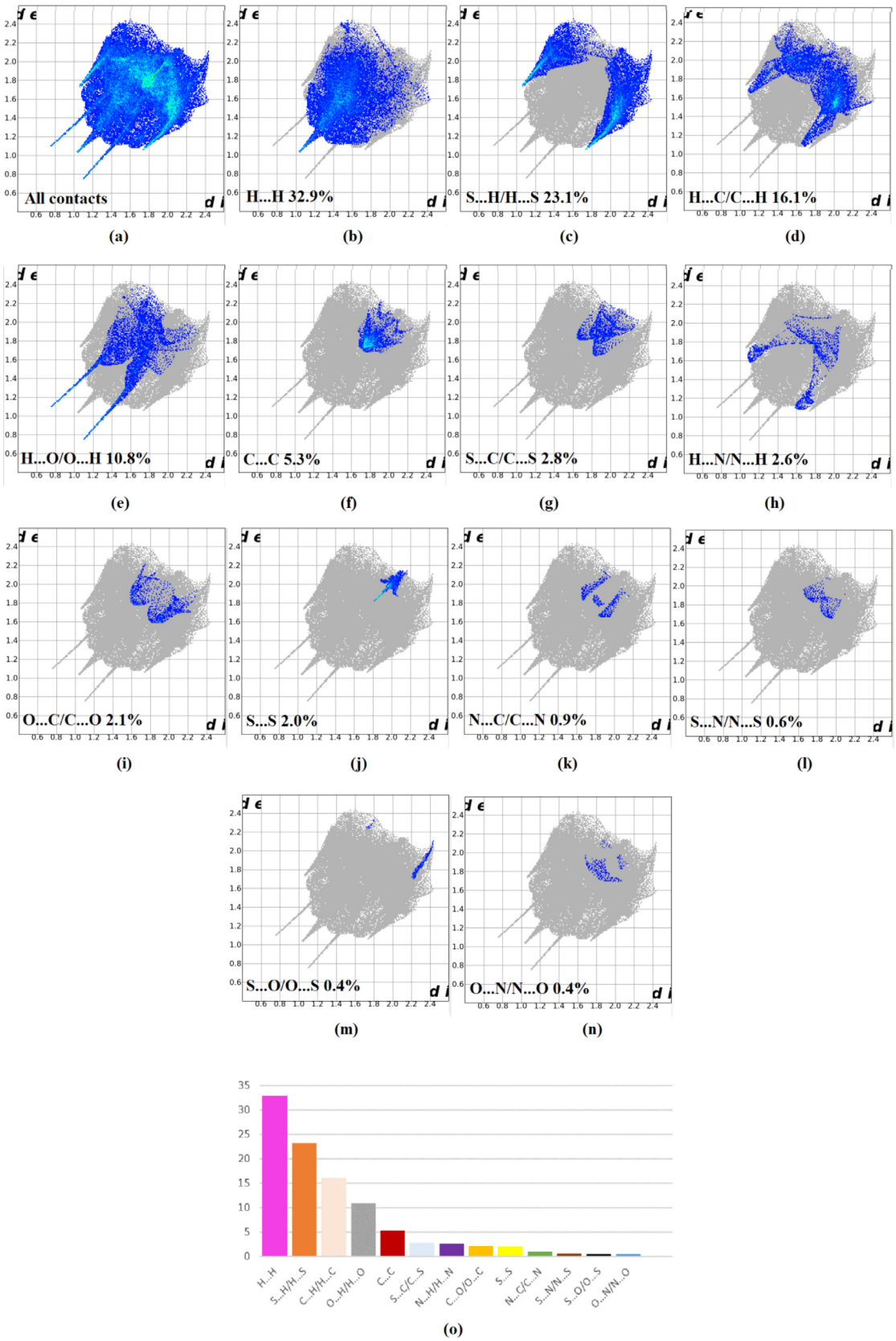

Fig. 10. Overall and decomposed 2D-FPs illustrating the relative contribution ratios of the contacts in (**I**).

Table 5
Grid parameters for each case.

Parameters	2Q85	4J7B
Size (Å)	60 × 60 × 60	60 × 60 × 60
Spacing (Å)	0.5	0.5
Coordinates	$x = 12.611$	$x = 6.542$
	$y = 0.120$	$y = -2.027$
	$z = 4.704$	$z = 26.966$

which exhibit a closest contact at (d_i = 1.15 Å and d_e = 0.76 Å) associated to the N1—H1···O1 hydrogen bond. In the crystal packing of (**I**), the C···C contacts contribute with a 5.3% value to the total **HS** and are mainly related to the $\pi-\pi$ staking. These contacts show a shortest interaction being approximately of 3.86 Å. As for the remaining contacts, namely S···C, N···H, O···C, S···S, N···C, S···N, S···O and N···O contacts, they are almost insignificant with a contribution of less than 2.8% (Fig. 9). The histogram of the relative contributions of all the intermolecular contacts existing in the crystal packing of (**I**) is shown in Fig. 10.o.

3.8. Molecular docking

The targets **2Q85** and **4J7B** were treated by removing the water molecules and the ligands from their crystal structures, then the polar hydrogen atoms were added. The Grid boxes were generated using the AutoGrid tool with 0.5 Å spacing and the grids' parameters are grouped in Table 5.

The best conformation with the lower binding energy in each case was considered, namely −7.45 and −6.25 Kcal/mol in respectively **2Q85** and **4J7B**. In Table 6, we illustrate the decomposed energies relating (**I**) to the receptors **2Q85** and **4J7B**.

Hydrogen bonds, hydrophobic and electrostatic interactions are crucial binding forces, which affect the molecular docking results and therefore the activity of the studied ligands against the targets. Consequently, compound (**I**) interacts with both receptors *via* hydrogen bonds displayed in Fig. 11. We have noticed that (**I**) forms two N—H···O hydrogen bonds with **2Q85** through the Glu_{323} residue (2.78 Å) as a donor and the Trp_{321} residue (2.69 Å) as an acceptor (Fig. 11.a). In the case of receptor **4J7B**, compound (**I**) interacts with it *via* five hydrogen-bonding interactions, namely one N—H···S and four N—H···O, formed with the following aminoacid residues: Leu_{276}, Lys_{580}, Asp_{277}, Asp_{278} and Leu_{315} as shown in Fig. 11.c. The geometric parameters of the observed H-bonds are listed in Table 7.

Additionally, the docking results showed the presence of other interactions in both cases and are summarized in Table 8. For receptor **2Q85**, π−anion interactions are resulting from Glu_{323} in addition to the $\pi-\sigma$ and the hydrophobic interactions linking (**I**) to the Val_{235} residue (Fig. 11.b). In the case of **4J7B**, these interactions are mainly $\pi-\pi$ stacking observed between (**I**) and the His_{313} residue. Furthermore, the ligand showed π-anion interactions linking its rhodanine ring to the Asp_{278} aminoacid's carbonyl group, hydrophobic interactions with Pro_{312} as well as Sulfur−*X*, π−cation and π−Sulfur interactions formed with the His_{313} aminoacid residue (Fig. 11.d).

3.9. ADMET properties

3.9.1. Absorption and physicochemical properties

The findings of the *in silico* ADME evaluation of compound (**I**) are shown in Table 9. The physicochemical properties play a major role in whether an active molecule could progress to be a successful drug candidate [79]. The absorption is the process of movement of a drug from an extravascular site of administration into the systemic circulation [80], which is resumed in lipophilicity and water solubility. Indeed, lipophilicity is known for its crucial significance in the drug development process [81, 82], as it is tightly connected to permeability through biological membranes. Therefore, permeability could decrease with the lipophilicity drop-off and most of the very hydrophilic molecules are unable to diffuse passively through the biological membranes [80]. Correspondingly, the partition coefficient between the immiscible n-octanol and water (LogPo/w) representing the lipophilicity classical descriptor was computed for (**I**) according to the fragmental XLOGP3 model [83], and was found to be 2.20 (Table 9). Furthermore, the estimation of an average of the five calculated topological and fragmental methods computed in Table 9, known as consensus LogPo/w, gave the value 1.35 indicating that compound (**I**) is slightly lipophilic. On the other hand, water-soluble molecules ease many drug development activities through their handling and formulation, and thus solubility in oral administration is considered a crucial property by influencing absorption [84]. In order to deliver a sufficient quantity of a drug's active ingredient, it has to be highly water-soluble which significantly affects its absorption and distribution characteristics [85]. Correspondingly, SwissADME estimated the molar solubility of (**I**) in water by computing the LogS (Silicos-IT) descriptor, being equal to −3.87 and signifying a good water-solubility of (**I**). Additionally, the estimation of the polar surface area (PSA) measuring apparent polarity through computing its topological PSA [86] returned a value of 96.52 $Å^2$, which suggests good intestinal absorption.

3.9.2. Distribution, metabolism and pharmacokinetic properties

Compound (**I**) showed a high predicted gastrointestinal absorption parameter (GIA), however it was found to be unable to cross the blood-brain barrier (BBB) partition. Therefore, the studied molecule could easily be absorbed in the intestines however its transit from the blood to the brain could not be allowed (Table 10). In fact, it was reported that a given molecule could more likely take part in drug-drug interactions (DDI) with other active molecules if it inhibits more CYP enzymes [87], especially the isoforms 1A2, 2C19, 2C9, 2D6 and 3A4 which are responsible of 90% for oxidative metabolic reactions [88]. Therefore, compound (**I**) was predicted to show no potency against these CYPs and to inhibit only the CYP1A2 isoform as well as the human P-glycoprotein transporter (Pgp) known to be involved in multiple drug resistance (MDR) and BBB penetration. Moreover, the studied molecule has shown a LogKp value of −6.34 cm/s which stands for low skin permeability [89].

3.9.3. Drug-likeness and bioavailability

Drug-likeness is defined by rules that evaluate qualitatively the chance for a given molecule to become a possible oral drug with respect to its bioavailability by considering ranges of specific physicochemical properties [60]. In fact, SwissADME gave access to five different rule-based filters, which originate from analyses by major pharmaceutical companies aiming to improve the quality of their proprietary chemical collections, namely the Lipinski [90], Veber [91], Egan [92], Muegge [93] and Ghose [94] methods. Particularly, the adopted criteria for the Lipinski's rule-of-five, considered the most famous rule-based filter allowing one to distinguish if a molecule could be orally absorbed, are a molecular weight (MW) $\leq$ 500, an octanol/water partition coefficient (MLOGP) $\leq$ 5, a number of hydrogen bond donors (HBDs) $\leq$ 5 and a number of hydrogen bond acceptors (HBAs) $\leq$ 10. Correspondingly, it can be seen from the results of Table 11 that molecule (**I**) violates none of the rules and could therefore be considered orally active. Furthermore, it displays a synthetic accessibility score of 2.78 which indicates an easy synthetic route, as well as a bioavailability score of 55% implying good bioavailability.

Table 6
Component terms of the lowest free binding energies (kcal/mol) of (**I**) with **2Q85** and **4J7B**.

	$\Delta G_{vdW} + \Delta G_{Hbond} + \Delta G_{desolv}$	ΔG_{elec}	$\Delta G_{intermol}$	$\Delta G_{tot\ int}$	ΔG_{tor}	$\Delta G_{unbound}$
2Q85	−7.97	−0.07	−8.04	−0.27	+0.60	−0.27
4J7B	−6.25	+0.05	−6.20	−0.36	+0.60	−0.36

With: $\Delta G_{intermol}$ is the final intermolecular energy ($\Delta G_{vdW} + \Delta G_{Hbond} + \Delta G_{desolv} + \Delta G_{elec}$),.
$\Delta G_{tot\ int}$ is the final total internal energy,.
ΔG_{tor} is the torsional free energy,.
$\Delta G_{unbound}$ is the unbound system's energy.

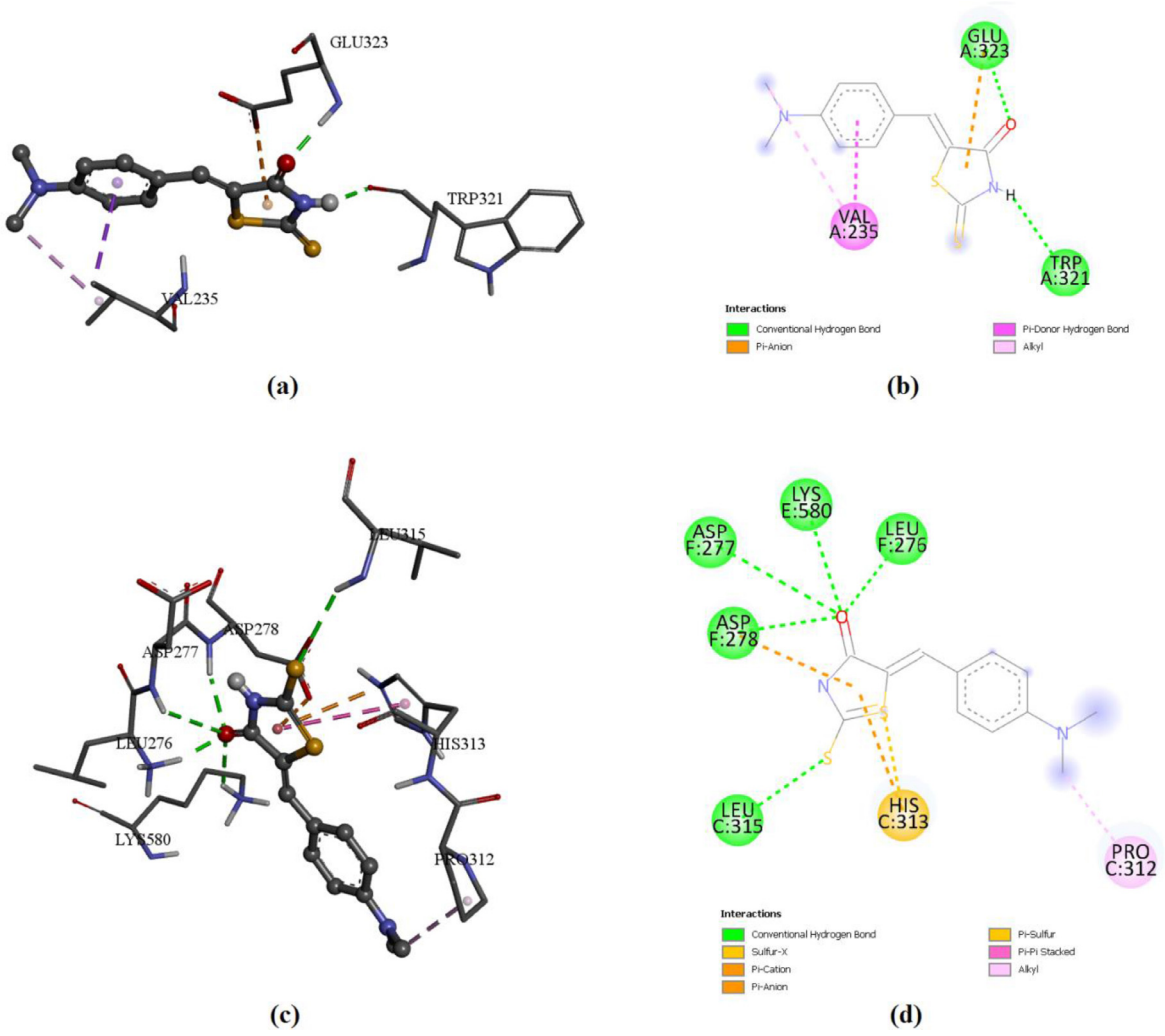

Fig. 11. Best docking poses showing compound (**I**) interacting with **(a)** and **(b) 2Q85**; and **(c)** and **(d) 4J7B** through H-bonds and the others interactions.

Table 7
Geometric parameters of hydrogen bonds formed in the binding pockets of **2Q85, 4J7B** and compound (**I**).

	Aminoacid residue	D–H···A	D···A (Å)	H···A (Å)
2Q85	Trp_{321}	N–H…O	2.69	2.11
	Glu_{323}	N–H…O	2.78	1.77
4J7B	Leu_{315}	N–H…S	2.89	1.91
	Leu_{276}	N–H…O	2.83	1.89
	Asp_{277}	N–H…O	3.45	3.02
	Asp_{278}	N–H…O	3.16	2.17
	Lys_{580}	N–H…O	3.36	2.53

Table 8
Interactions' types linking ligand (**I**) to receptors **2Q85** and **4J7B**.

Receptors	$\pi-\pi$ stacking	$\pi-\sigma$	Sulfur–X	$\pi-$cation	$\pi-$anion	$\pi-$Sulfur	$\pi-$Alkyl	Alkyl
2Q85	/	Val_{235}	/	/	Glu_{323}	/	/	Val_{235}
4J7B	His_{313}	/	His_{313}	His_{313}	Asp_{278}	His_{313}	/	Pro_{312}

Table 9
Physicochemical properties estimated for (**I**).

Physicochemical Properties	
Formula	$C_{12}H_{12}N_2OS_2$
M.W	264.37 g/mol
Fraction Csp3	0.25
NROT	3
HBA	1
HBD	1
MR	80.42
TPSA	96.52 Å²
Lipophilicity	
Log Po/w (iLOGP)	0.00
Log Po/w (XLOGP3)	2.20
Log Po/w (WLOGP)	1.28
Log Po/w (MLOGP)	1.28
Log Po/w (SILICOS-IT)	1.97
Consensus Log Po/w	1.35
Water Solubility	
Log S (ESOL)	−2.93
Solubility	$3.07e^{-01}$ mg/mL; $1.16e^{-03}$ mol/L
Class	Soluble
Log S (Ali)	−3.87
Solubility	$3.55e^{-02}$ mg/mL; $1.34e^{-04}$ mol/L
Class	Soluble
Log S (SILICOS-IT)	−3.87
Solubility	$3.54e^{-02}$ mg/mL; $1.34e^{-04}$ mol/L
Class	Soluble

MW: molecular weight; NROT: No. of rotating bonds; HBA: No. of H-bond acceptors;.
HBD: No. of H-bond donors; MR: Molar Refractivity; TPSA: Topological polar surface area.

Table 10
Predicted pharmacokinetic properties of (**I**).

Pharmacokinetics	
GIA	High
BBB permeant	No
P-gp substrate	No
CYP1A2 inhibitor	Yes
CYP2C19 inhibitor	No
CYP2C9 inhibitor	No
CYP2D6 inhibitor	No
CYP3A4 inhibitor	No
Log Kp (skin permeation)	−6.34 cm/s

GIA: gastrointestinal absorption; BBB: blood-brain barrier;.
CYP: Cytochrome P450; P-gp substrate: Glycoprotein substrate P.

Table 11
Drug-likeness profile and medicinal properties calculated for the studied molecule.

Drug-likeness		Medicinal Chemistry	
Lipinski	Yes;	PAINS	1 alert : thio_ketone
Ghose	Yes	Brenk	1 alert : thio-carbonyl_group
Veber	Yes	Lead-likeness	Yes
Egan	Yes	Synthetic accessibility 2.78	
Muegge	Yes		
Bio-availability Score 0.55			

Moreover, the oral bioavailability radar (OBR) of compound (**I**), considered a rapid appraisal of drug-likeness, is depicted in Fig. 12 by taking into consideration the six physicochemical properties ; namely the lipophilicity (lipo), size, polarity (polar), insolubility (insolu), flexibility (flex) and unsaturation (insatu). Consequently, the OBR is illustrated as a radar plot of compound (**I**) which falls entirely inside the pink area representing the optimal range of the mentioned descriptors, thus indicating that the studied molecule could be considered drug-like.

3.9.4. Toxicity properties

The predicted toxicity properties of compound (**I**) given in Table 12 showed no human ether-a-go-go-related gene (hERG) potassium channel inhibition, resulting thus in no risk of cardiotoxicity and no cardiac side effects which represent a major problem in clinical studies of drug candidates [95]. Furthermore, (**I**)

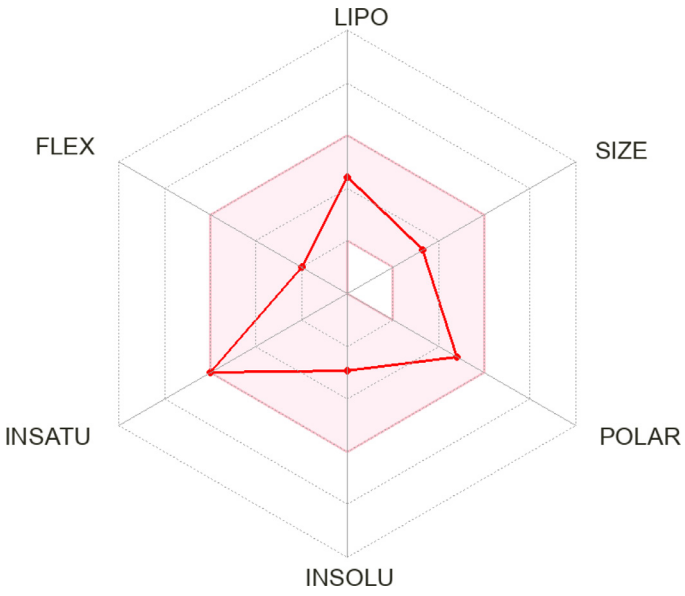

Fig. 12. Appropriate profile of the oral bioavailability radar of (**I**). The colored zone is the appropriate physical-chemical space for oral bioavailability.

Table 12
Toxicity properties estimated for (**I**).

Toxicity		
hERG	Weak inhibitor	0.9832
Inhibition	Non-inhibitor	0.8553
AMES Toxicity	Non AMES toxic	0.6860
Carcinogens	Non-carcinogens	0.8423
Fish Toxicity	High FHMT	0.8512
Tetrahymena Pyriformis Toxicity	High TPT	0.6926
Honey Bee Toxicity	Low HBT	0.6617
Biodegradation	Not ready biodegradable	1.0000
Acute Oral Toxicity AO	III	0.6594
Carcinogenicity (Three-class)	Non-required	0.5062

hERG: Human Ether-a-go-go-Related Gene.

showed no Ames toxicity which should be evaluated in the early stages of drug discovery in order to estimate the potential genotoxicity of the studied molecule. As for the calculated acute oral toxicity AO of (**I**), it was estimated to be 659.4 mg.kg^{-1}, which falls in the 3rd category being in the range (500 mg.kg^{-1} < LD50 ≤ 5000 mg.kg^{-1}) and thus makes it a nontoxic molecule [96]. Additionally, a value of 506.2 mg.kg^{-1} body-weight per day was predicted for the carcinogenicity descriptor (CARC) [97], which indicates that (**I**) could be considered non-carcinogenic.

4. Conclusions

To the best of our knowledge, this study is the first to report the crystal structure for the rhodanine derivative 5-(4-dimethylaminobenzylidene)rhodanine, compound (**I**). The studied compound, orange/red thin slabs, crystallizes in the monoclinic $P2_1/c$ space group and its asymmetric unit encloses one molecule. The related absorption and luminescence spectra were collected on single-crystals under a modified optical microscope. Optical absorption exhibits an onset at around 2.0 eV and its first maximum at ∼2.25 eV. The luminescence is well-structured, peaked at 2.01 eV, and it shows a vibronic progression of 1240 cm^{-1} constructed on its origin, associated to the C = S stretching. Furthermore, compound (**I**) was optimized by DFT methods, which reproduced well its geometric parameters. IR vibrational wavenumbers and ^{1}H and ^{13}C NMR chemical shifts were computed and compared to the experimental values. The frontier molecular orbitals were then estimated and evaluated. In addition, TD-DFT was employed to explore the absorption spectra. The structural features of (**I**) were furthermore investigated by carrying out a **HSA**, which showed with its subsequent 2D-**FP**s that the prominent intermolecular interactions in the structure are the C—H···O and C–H···N hydrogen bonds as well as the C—H···H—C, C—H···π, π···*lp* interactions and the $\pi-\pi$ stacking. Furthermore, the *in silico* study performed by docking (**I**) against the Polo-like kinase PLK1 and the *E. coli* MurB enzymes showed the presence of N—H···O hydrogen-bonding, π−anion, $\pi-\sigma$, hydrophobic interactions with **2Q85**, as well as N—H···O, N—H···S hydrogen-bonding, π−anion, Sulfur−*X*, π−cation, π−Sulfur, hydrophobic interactions and $\pi-\pi$ stacking with **4J7B**. As a result, the studied compound might be a potential agent for cancer progression's prevention and *E. coli* inhibition. As for the conducted ADMET predictions, they showed that (**I**) is water-soluble and slightly lipophilic. Moreover, compound (**I**) displayed a good intestinal absorption and showed no cardiotoxicity risk, which therefore makes it a potential drug-like molecule.

Declaration of Competing Interest

The authors declare that they have no known competing financial interests or personal relationships that could have appeared to influence the work reported in this paper.

CRediT authorship contribution statement

Amal Guerraoui: Resources, Methodology. **Meriem Goudjil:** Data curation, Formal analysis, Methodology, Software, Validation, Writing – review & editing. **Amani Direm:** Software, Supervision, Validation, Writing – review & editing. **Abdenour Guerraoui:** Conceptualization, Software, Methodology, Writing – original draft. **İlkin Yücel Şengün:** Software, Validation, Writing – review & editing. **Cemal Parlak:** Software, Validation, Writing – review & editing. **Amel Djedouani:** Funding acquisition, Investigation, Supervision. **Laura Chelazzi:** Methodology, Validation. **Filippo Monti:** Methodology, Writing – review & editing. **Eugenio Lunedei:** Methodology, Writing – review & editing. **Abdecharif Boumaza:** Funding acquisition, Investigation, Supervision.

Data Availability

No data was used for the research described in the article.

Acknowledgements

The authors would like to acknowledge the fund of the Ministry of Higher Education and Scientific Research MESRS and Abbes Laghrour University of Khenchela (Algeria) under the project number: B00L01UN400120210002 (PRFU). M.G. thanks CRIST: Centro di Servizi di Cristallografia Strutturale, University of Florence (Italy). E.L. acknowledges S.Bonetti (CNR-ISMN, Bologna) for his help in building the micro-spectroscopy setup. The authors acknowledge Fencluster system of Ege University (Turkey) for the calculations.

Supplementary materials

Supplementary material associated with this article can be found, in the online version, at doi:10.1016/j.molstruc.2023.135025.

References

[1] A. Verma, S.K. Saraf, 4-Thiazolidinone–A biologically active scaffold, Eur. J. Med. Chem. 43 (5) (2008) 897–905.
[2] A.K. Jain, A. Vaidya, V. Ravichandran, S.K. Kashaw, R.K. Agrawal, Recent developments and biological activities of thiazolidinone derivatives: a review, Bioorg. Med. Chem. 20 (11) (2012) 3378–3395.
[3] J. Dwivedi, K. Devi, Y. Asmat, S. Jain, S. Sharma, Synthesis, characterization, antibacterial and antiepileptic studies of some novel thiazolidinone derivatives, J. Saudi Chem. Soc. 20 (2016) S16–S20.
[4] S. Ashraf, A. Saeed, S.H. Moon, U. Flörke, S.H. Kim, Z. Ashraf, M. Yaseen, M. Latif, Design, synthesis and biological evaluation of 2-(naphthoyl) iminothiazolidin-4-ones as potential anticancer agents, ChemistrySelect. 5 (13) (2020) 3965–3970.
[5] Y.S. Prabhakar, V. Raja Solomon, M.K. Gupta, S. Katti, QSAR studies on thiazolidines: a biologically privileged scaffold, in: QSAR and Molecular Modeling Studies in Heterocyclic Drugs II, 2006, pp. 161–249.
[6] I. Khan, A. Ibrar, N. Abbas, Triazolothiadiazoles and triazolothiadiazines–biologically attractive scaffolds, Eur. J. Med. Chem. 63 (2013) 854–868.
[7] Ş.H. Üngören, S. Albayrak, A. Günay, L. Yurtseven, N. Yurttaş, A new method for the preparation of 5-acylidene and 5-imino substituted rhodanine derivatives and their antioxidant and antimicrobial activities, Tetrahedron 71 (25) (2015) 4312–4323.
[8] H. Zhou, S. Wu, S. Zhai, A. Liu, Y. Sun, R. Li, Y. Zhang, S. Ekins, P.W. Swaan, B. Fang, Design, synthesis, cytoselective toxicity, structure–activity relationships, and pharmacophore of thiazolidinone derivatives targeting drug-resistant lung cancer cells, J. Med. Chem. 51 (5) (2008) 1242–1251.
[9] D. Havrylyuk, B. Zimenkovsky, O. Vasylenko, L. Zaprutko, A. Gzella, R. Lesyk, Synthesis of novel thiazolone-based compounds containing pyrazoline moiety and evaluation of their anticancer activity, Eur. J. Med. Chem. 44 (4) (2009) 1396–1404.
[10] D. Kaminskyy, D. Khyluk, O. Vasylenko, L. Zaprutko, R. Lesyk, A facile synthesis and anticancer activity evaluation of spiro [thiazolidinone-isatin] conjugates, Sci. Pharm. 79 (4) (2011) 763–778.

[11] J. Balzarini, B. Orzeszko, J.K. Maurin, A. Orzeszko, Synthesis and anti-HIV studies of 2-adamantyl-substituted thiazolidin-4-ones, Eur. J. Med. Chem. 42 (7) (2007) 993–1003.

[12] J.L. Romine, D.R. St. Laurent, J.E. Leet, S.W. Martin, M.H. Serrano-Wu, F. Yang, M. Gao, D.R. O'Boyle, J.A. Lemm, J.-.H. Sun, Inhibitors of HCV NS5A: from iminothiazolidinones to symmetrical stilbenes, ACS Med. Chem. Lett. 2 (3) (2011) 224–229.

[13] N. Ulusoy, N. Ergenç, A. Ekinci, H. Özer, Synthesis and anticonvulsant activity of some new arylidenehydrazides and 4-thiazolidinones, Monatshefte für Chemie/Chemical Monthly 127 (11) (1996) 1197–1202.

[14] J. Joy, N. Jacob, G. Kutty, Evaluation of hypoglycemic effects of 4-thiazolidinones, Indian Drugs 42 (1) (2005) 17–21.

[15] D. Kaminskyy, A. Kryshchyshyn, R. Lesyk, Recent developments with rhodanine as a scaffold for drug discovery, Expert Opin. Drug Discov. 12 (12) (2017) 1233–1252.

[16] A. Hara, T. Suzuki, H. Hashizume, N. Shishido, M. Nakamura, F. Ushikubi, Y. Abiko, Effects of CP-060S, a novel Ca^{2+} channel blocker, on oxidative stress in cultured cardiac myocytes, Eur. J. Pharmacol. 385 (1) (1999) 81–88.

[17] K.H. Inoue, A.E. Hagerman, Determination of gallotannin with rhodanine, Anal. Biochem. 169 (2) (1988) 363–369.

[18] T. Tomasic, L.P. Masic, Rhodanine as a privileged scaffold in drug discovery, Curr. Med. Chem. 16 (13) (2009) 1596–1629.

[19] R. Lesyk, B. Zimenkovsky, 4-Thiazolidones: centenarian history, current status and perspectives for modern organic and medicinal chemistry, Curr. Org. Chem. 8 (16) (2004) 1547–1577.

[20] M. Metwally, A.A. Farahat, B.F. Abdel-Wahab, 2-Amino-4-thiazolidinones: synthesis and reactions, J. Sulfur Chem. 31 (4) (2010) 315–349.

[21] A. Andreani, M. Rambaldi, A. Leoni, A. Locatelli, R. Bossa, M. Chiericozzi, I. Galatulas, G. Salvatore, Synthesis and cardiotonic activity of imidazo [2, lb] thiazoles bearing a lactam ring, Eur. J. Med. Chem. 31 (5) (1996) 383–387.

[22] Y. Hu, J.S. Helm, L. Chen, C. Ginsberg, B. Gross, B. Kraybill, K. Tiyanont, X. Fang, T. Wu, S. Walker, Identification of selective inhibitors for the glycosyltransferase MurG via high-throughput screening, Chem. Biol. 11 (5) (2004) 703–711.

[23] J.H. Ahn, S.J. Kim, W.S. Park, S.Y. Cho, J. Du Ha, S.S. Kim, S.K. Kang, D.G. Jeong, S.-.K. Jung, S.-.H. Lee, Synthesis and biological evaluation of rhodanine derivatives as PRL-3 inhibitors, Bioorg. Med. Chem. Lett. 16 (11) (2006) 2996–2999.

[24] J.B. Baell, Observations on screening-based research and some concerning trends in the literature, Fut. Med. Chem. 2 (10) (2010) 1529–1546.

[25] M.d.l.A.A. Pérez, L.L. Duharte, Y.P. Ramírez, S.L. Yánez, Highly selective PVC-membrane electrodes based on 5-(4-Dimethylamino) benzylidene) Rhodanine for determination of silver ion, Revista Cubana de Química 22 (1) (2010) 17–21.

[26] M.d.l.A.A. Pérez, L.L. Duhartea, M. Yazdani-Pedramb, Study and characterization of a silver-selective membrane electrode based on 5-(4-dimethylaminobenzylidene) rhodanine, Portugaliae Electrochimica Acta 37 (6) (2019) 373–382.

[27] D.M. Glover, I.M. Hagan, Á.A. Tavares, Polo-like kinases: a team that plays throughout mitosis, Gene Dev. 12 (24) (1998) 3777–3787.

[28] F.A. Barr, H.H. Silljé, E.A. Nigg, Polo-like kinases and the orchestration of cell division, Nat. Rev. Mol. Cell Biol. 5 (6) (2004) 429–441.

[29] V. Archambault, D.M. Glover, Polo-like kinases: conservation and divergence in their functions and regulation, Nat. Rev. Mol. Cell Biol. 10 (4) (2009) 265–275.

[30] B. Song, X.S. Liu, X. Liu, Polo-like kinase 1 (Plk1): an unexpected player in DNA replication, Cell Div. 7 (1) (2012) 1–7.

[31] H.A. Lane, E.A. Nigg, Antibody microinjection reveals an essential role for human polo-like kinase 1 (Plk1) in the functional maturation of mitotic centrosomes, J. Cell Biol. 135 (6) (1996) 1701–1713.

[32] I.M. Brennan, U. Peters, T.M. Kapoor, A.F. Straight, Polo-like kinase controls vertebrate spindle elongation and cytokinesis, PLoS One 2 (5) (2007) e409.

[33] L.-.Y. Lu, J.L. Wood, K. Minter-Dykhouse, L. Ye, T.L. Saunders, X. Yu, J. Chen, Polo-like kinase 1 is essential for early embryonic development and tumor suppression, Mol. Cell. Biol. 28 (22) (2008) 6870–6876.

[34] G. de Cárcer, G. Manning, M. Malumbres, From Plk1 to Plk5: functional evolution of polo-like kinases, Cell Cycle 10 (14) (2011) 2255–2262.

[35] Y.H. Kang, C.H. Park, T.-.S. Kim, N.-.K. Soung, J.K. Bang, B.Y. Kim, J.-.E. Park, K.S. Lee, Mammalian polo-like kinase 1-dependent regulation of the PBIP1-CENP-Q complex at kinetochores, J. Biol. Chem. 286 (22) (2011) 19744–19757.

[36] J.R. Bader, J.M. Kasuboski, M. Winding, P.S. Vaughan, E.H. Hinchcliffe, K.T. Vaughan, Polo-like kinase1 is required for recruitment of dynein to kinetochores during mitosis, J. Biol. Chem. 286 (23) (2011) 20769–20777.

[37] R.F. Lera, M.E. Burkard, High mitotic activity of Polo-like kinase 1 is required for chromosome segregation and genomic integrity in human epithelial cells, J. Biol. Chem. 287 (51) (2012) 42812–42825.

[38] J. Zhang, L. Zhang, J. Wang, L. Ouyang, Y. Wang, Polo-like kinase 1 inhibitors in human cancer therapy: development and therapeutic potential, J. Med. Chem. 65 (15) (2022) 10133–10160.

[39] Y. Ding, H. Liu, C. Zhang, Z. Bao, S. Yu, Polo-like kinases as potential targets and PLK2 as a novel biomarker for the prognosis of human glioblastoma, Aging 14 (5) (2022) 2320.

[40] U. Holtrich, G. Wolf, A. Bräuninger, T. Karn, B. Böhme, H. Rübsamen-Waigmann, K. Strebhardt, Induction and down-regulation of PLK, a human serine/threonine kinase expressed in proliferating cells and tumors, Proc. Natl. Acad. Sci. 91 (5) (1994) 1736–1740.

[41] P. Ramani, R. Nash, E. Sowa-Avugrah, C. Rogers, High levels of polo-like kinase 1 and phosphorylated translationally controlled tumor protein indicate poor prognosis in neuroblastomas, J. Neuro-Oncol. 125 (1) (2015) 103–111.

[42] T.G. Tut, S. Lim, I.U. Dissanayake, J. Descallar, W. Chua, W. Ng, P. de Souza, J.-.S. Shin, C.S. Lee, Upregulated polo-like kinase 1 expression correlates with inferior survival outcomes in rectal cancer, PLoS One 10 (6) (2015) e0129313.

[43] K.E. Arnst, S. Banerjee, H. Chen, S. Deng, D.J. Hwang, W. Li, D.D. Miller, Current advances of tubulin inhibitors as dual acting small molecules for cancer therapy, Med. Res. Rev. 39 (4) (2019) 1398–1426.

[44] Y. Zhang, Z. Guo, X.-.Z. You, Hydrolysis theory for cisplatin and its analogues based on density functional studies, J. Am. Chem. Soc. 123 (38) (2001) 9378–9387.

[45] S.J.Y. Macalino, V. Gosu, S. Hong, S. Choi, Role of computer-aided drug design in modern drug discovery, Arch. Pharm. Res. 38 (9) (2015) 1686–1701.

[46] A. Bruker, SAINT and SADABS, Bruker Analytical X-ray, Systems. Inc., Madison, Wisconsin, USA, 2008.

[47] G.M. Sheldrick, SHELXT–Integrated space-group and crystal-structure determination, Acta Crystallogr. Sect. A 71 (1) (2015) 3–8.

[48] G.M. Sheldrick, Crystal structure refinement with SHELXL, Acta Crystallogr. Sect. C 71 (1) (2015) 3–8.

[49] O.V. Dolomanov, L.J. Bourhis, R.J. Gildea, J.A. Howard, H. Puschmann, *OLEX2*: a complete structure solution, refinement and analysis program, J. Appl. Crystallogr. 42 (2) (2009) 339–341.

[50] D. Avci, Y. Atalay, Theoretical analysis of vibrational spectra and scaling-factor of 2-aryl-1,3,4-oxadiazole derivatives, Int. J. Quantum Chem. 109 (2) (2009) 328–341, doi:10.1002/qua.21789.

[51] J. Tomasi, B. Mennucci, R. Cammi, Quantum mechanical continuum solvation models, Chem. Rev. 105 (2005) 2999–3093.

[52] A. Dreuw, M. Head-Gordon, Single-reference ab initio methods for the calculation of excited states of large molecules, Chem. Rev. 105 (11) (2005) 4009–4037, doi:10.1021/cr0505627.

[53] K. Wolinski, J.F. Hinton, P. Pulay, Efficient implementation of the gauge-independent atomic orbital method for NMR chemical shift calculations, J. Am. Chem. Soc. 112 (23) (1990) 8251–8260.

[54] R.D. Dennington, T.A. Keith, J.M. Millam, GaussView 6.0.16, Gaussian Inc., 2016.

[55] M.J. Frisch, G.W. Trucks, H.B. Schlegel, et al., Gaussian 16, Revision C.01, Gaussian Inc., Wallingford, CT, 2016.

[56] P.R. Spackman, M.J. Turner, J.J. McKinnon, S.K. Wolff, D.J. Grimwood, D. Jayatilaka, M.A. Spackman, CrystalExplorer: a program for Hirshfeld surface analysis, visualization and quantitative analysis of molecular crystals, J. Appl. Crystallogr. 54 (3) (2021) 1006–1011.

[57] G.M. Morris, R. Huey, W. Lindstrom, M.F. Sanner, R.K. Belew, D.S. Goodsell, A.J. Olson, AutoDock4 and AutoDockTools4: automated docking with selective receptor flexibility, J. Comput. Chem. 30 (16) (2009) 2785–2791.

[58] H.M. Berman, J. Westbrook, Z. Feng, G. Gilliland, T.N. Bhat, H. Weissig, I.N. Shindyalov, P.E. Bourne, The protein data bank, Nucleic Acids Res. 28 (1) (2000) 235–242.

[59] B. Biovia, Dassault Systèmes, Discovery Studio Visualizer, v21. 1.0. 20298, Dassault Systèmes, San Diego, CA, USA, 2021.

[60] A. Daina, O. Michielin, V. Zoete, SwissADME: a free web tool to evaluate pharmacokinetics, drug-likeness and medicinal chemistry friendliness of small molecules, Sci. Rep. 7 (1) (2017) 1–13.

[61] F. Cheng, W. Li, Y. Zhou, J. Shen, Z. Wu, G. Liu, P.W. Lee, Y. Tang, admetSAR: a Comprehensive Source and Free Tool for Assessment of Chemical ADMET Properties, ACS Publications, 2012.

[62] J. Bernstein, R.E. Davis, L. Shimoni, N.L. Chang, Patterns in hydrogen bonding: functionality and graph set analysis in crystals, Angew. Chem. Int. Ed. 34 (15) (1995) 1555–1573.

[63] K. Balakumaran, J. Mosesbabu, J. Anireddy, G. Chakkaravarthi, (E)-5-{4-[2-(5-Ethylpyridin-2-yl) ethoxy] benzylidene} thiazolidine-2, 4-dione, IUCrData 3 (1) (2018) x171839.

[64] A. Guerraoui, A. Djedouani, E. Jeanneau, A. Boumaza, A. Alsalme, A. Zarrouk, K.S. Salih, I. Warad, Crystal structure and spectral of new hydrazine-pyran–dione derivative: DFT enol↔ hydrazone tautomerization via zwitterionic intermediate, hirshfeld analysis and optical activity studies, J. Mol. Struct. 1220 (2020) 128728.

[65] R. El Ajlaoui, E.M. Rakib, M. Chigr, M. Saadi, L. El Ammari, Crystal structure of (Z)-3-allyl-5-(4-methylbenzylidene)-2-sulfanylidene-1, 3-thiazolidin-4-one, Acta Crystallogr. Sect. E 71 (Pt 12) (2015) o906.

[66] R. El Ajlaoui, E. Rakib, S. Mojahidi, M. Saadi, L. El Ammari, (Z)-3-Allyl-5-(3-methoxybenzylidene)-2-sulfanylidene-1, 3-thiazolidin-4-one, IUCrData 1 (1) (2016) x160052.

[67] D. Shahwar, M.A. Raza, S. Aslam, S. Mehmood, S. Tariq, A.M. Asiri, 3-Benzyl-5-benzylidene-2-sulfanylidene-1, 3-thiazolidin-4-one, Acta Crystallogr. Sect. E 67 (8) (2011) o2083.

[68] D. Shahwar, M.N. Tahir, M. Kashif, A. Saeed, S. Bukhari, (5Z)-5-(2-Hydroxybenzylidene)-3-(4-methylphenyl)-2-sulfanylidene-1, 3-thiazolidin-4-one, Acta Crystallogr. Sect. E 68 (6) (2012) o1818.

[69] A. Insuasty, B. Insuasty, J. Cobo, C. Glidewell, Z)-5-[4-(Dimethylamino) benzylidene]-2-(piperidin-1-yl)-1, 3-thiazolidin-4 (5H)-one, Acta Crystallogr. Sect. C 69 (1) (2013) 74–76.

[70] V.Q. Trung, N.N. Linh, T.T.T. Duong, N.T. Chinh, D.K. Linh, H.M. Hung, D.T.Y. Oanh, Synthesis and characterization of novel poly [4-phenyl-3-(thiophen-3-ylmethyl)-1H-1, 2, 4-triazole-5 (4H)-thione], Vietnam J. Chem. 57 (6) (2019) 770–776.

[71] R. Anbarasan, A. Dhandapani, S. Manivarman, S. Subashchandrabose, H. Saleem, Synthesis and spectroscopical study of rhodanine derivative using DFT approaches, Spectrochim. Acta Part A 146 (2015) 261–272.
[72] Ö. Alver, C. Parlak, M. Şenyel, FT-IR and NMR investigation of 1-phenylpiperazine: a combined experimental and theoretical study, Spectrochim. Acta Part A 67 (3–4) (2007) 793–801.
[73] A. Salcı, R. Solmaz, Fabrication of rhodanine self-assembled monolayer thin films on copper: solvent optimization and corrosion inhibition studies, Prog. Org. Coat. 125 (2018) 516–524.
[74] A. Insuasty, A. Ortiz, A. Tigreros, E. Solarte, B. Insuasty, N. Martín, 2-(1, 1-dicyanomethylene) rhodanine: a novel, efficient electron acceptor, Dyes Pigm. 88 (3) (2011) 385–390.
[75] L.H. Madkour, S. Kaya, L. Guo, C. Kaya, Quantum chemical calculations, molecular dynamic (MD) simulations and experimental studies of using some azo dyes as corrosion inhibitors for iron. Part 2: Bis–azo dye derivatives, J. Mol. Struct. 1163 (2018) 397–417.
[76] A. Ghosh, A. Sarkar, P. Mitra, A. Banerji, J. Banerji, S. Mandal, M. Das, Crystal structure and DFT calculations of 3, 4-seco-lup-20 (29)-en-3-oic acid isolated from Wrightia tinctoria: stacking of supramolecular dimers in the crystal lattice, J. Mol. Struct. 980 (1–3) (2010) 7–12.
[77] J. Kawakami, H. Kakinami, N. Matsushima, A. Nakane, H. Kitahara, M. Nagaki, S. Ito, Structure–activity relationship analysis for Antimicrobial activities of Tryptanthrin derivatives using quantum chemical calculations, J. Comput. Chem. (2013) 2012-0026.
[78] S. Alyar, T. Şen, Ü.Ö. Özmen, H. Alyar, Ş. Adem, C. Şen, Synthesis, spectroscopic characterizations, enzyme inhibition, molecular docking study and DFT calculations of new Schiff bases of sulfa drugs, J. Mol. Struct. 1185 (2019) 416–424.
[79] E. Kwong, Oral Formulation Roadmap from Early Drug Discovery to Development, John Wiley & Sons, 2017.
[80] D. Lagorce, D. Douguet, M.A. Miteva, B.O. Villoutreix, Computational analysis of calculated physicochemical and ADMET properties of protein-protein interaction inhibitors, Sci. Rep.-Uk 7 (1) (2017) 1–15.
[81] V. Pliška, B. Testa, H. van de Waterbeemd, R. Mannhold, H. Kubinyi, H. Timmerman, Lipophilicity in Drug Action and Toxicology, Wiley Online Library, 1996.
[82] J.A. Arnott, S.L. Planey, The influence of lipophilicity in drug discovery and design, Expert Opin. Drug Discov. 7 (10) (2012) 863–875.
[83] T. Cheng, Y. Zhao, X. Li, F. Lin, Y. Xu, X. Zhang, Y. Li, R. Wang, L. Lai, Computation of octanol– water partition coefficients by guiding an additive model with knowledge, J. Chem. Inf. Model. 47 (6) (2007) 2140–2148.
[84] T.J. Ritchie, S.J. Macdonald, S. Peace, S.D. Pickett, C.N. Luscombe, Increasing small molecule drug developability in sub-optimal chemical space, Medchemcomm 4 (4) (2013) 673–680.
[85] K.T. Savjani, A.K. Gajjar, J.K. Savjani, Drug solubility: Importance and Enhancement Techniques, International Scholarly Research Notices, 2012 2012.
[86] P. Ertl, B. Rohde, P. Selzer, Fast calculation of molecular polar surface area as a sum of fragment-based contributions and its application to the prediction of drug transport properties, J. Med. Chem. 43 (20) (2000) 3714–3717.
[87] F. Cheng, Y. Yu, J. Shen, L. Yang, W. Li, G. Liu, P.W. Lee, Y. Tang, Classification of cytochrome P450 inhibitors and noninhibitors using combined classifiers, J. Chem. Inf. Model. 51 (5) (2011) 996–1011.
[88] J.A. Williams, R. Hyland, B.C. Jones, D.A. Smith, S. Hurst, T.C. Goosen, V. Peterkin, J.R. Koup, S.E. Ball, Drug-drug interactions for UDP-glucuronosyltransferase substrates: a pharmacokinetic explanation for typically observed low exposure (AUCi/AUC) ratios, Drug Metabol. Disposit. 32 (11) (2004) 1201–1208.
[89] P. Ro, Guy, Predicting skin permeability, Pharm. Res. 9 (5) (1992) 663–669.
[90] C.A. Lipinski, F. Lombardo, B.W. Dominy, P.J. Feeney, Experimental and computational approaches to estimate solubility and permeability in drug discovery and development settings, Adv. Drug Deliver. Rev. 23 (1–3) (1997) 3–25.
[91] D.F. Veber, S.R. Johnson, H.-.Y. Cheng, B.R. Smith, K.W. Ward, K.D. Kopple, Molecular properties that influence the oral bioavailability of drug candidates, J. Med. Chem. 45 (12) (2002) 2615–2623.
[92] W.J. Egan, K.M. Merz, J.J. Baldwin, Prediction of drug absorption using multivariate statistics, J. Med. Chem. 43 (21) (2000) 3867–3877.
[93] I. Muegge, S.L. Heald, D. Brittelli, Simple selection criteria for drug-like chemical matter, J. Med. Chem. 44 (12) (2001) 1841–1846.
[94] A.K. Ghose, V.N. Viswanadhan, J.J. Wendoloski, A knowledge-based approach in designing combinatorial or medicinal chemistry libraries for drug discovery. 1. A qualitative and quantitative characterization of known drug databases, J. Comb. Chem. 1 (1) (1999) 55–68.
[95] S. Wang, Y. Li, J. Wang, L. Chen, L. Zhang, H. Yu, T. Hou, ADMET evaluation in drug discovery. 12. Development of binary classification models for prediction of hERG potassium channel blockage, Mol. Pharmaceut. 9 (4) (2012) 996–1010.
[96] X. Li, L. Chen, F. Cheng, Z. Wu, H. Bian, C. Xu, W. Li, G. Liu, X. Shen, Y. Tang, In silico prediction of chemical acute oral toxicity using multi-classification methods, J. Chem. Inf. Model. 54 (4) (2014) 1061–1069.
[97] X. Li, Z. Du, J. Wang, Z. Wu, W. Li, G. Liu, X. Shen, Y. Tang, In silico estimation of chemical carcinogenicity with binary and ternary classification methods, Mol. Inform. 34 (4) (2015) 228–235.